Comprehensive Summaries of Uppsala Dissertations
from the Faculty of Medicine 1034

Quantitative Imaging with PET

Performance and Applications of ^{76}Br, ^{52}Fe, ^{110m}In and ^{134}La

BY

MARK LUBBERINK

ACTA UNIVERSITATIS UPSALIENSIS
UPPSALA 2001

Quantitative imaging with PET

Performance and Applications of ^{76}Br, ^{52}Fe, ^{110m}In and ^{134}La.

MARK LUBBERINK

Version: 27-3-2001

Dissertation for the Degree of Doctor of Philosophy (Faculty of Medicine) in Medical Radiation Physics presented at Uppsala University in 2001

ABSTRACT

Lubberink, M. 2001. Quantitative Imaging with PET. Performance and Applications of ^{76}Br, ^{52}Fe, ^{110m}In and ^{134}La. Acta Universitatis Uppsaliensis. *Comprehensive Summaries of Uppsala Dissertations from the Faculty of Medicine* 1034. 82 pp. Uppsala. ISBN 91-554-5015-6.

The use of positron emission tomography (PET) has so far been limited to a few nuclides with short half-lives such as ^{18}F and ^{11}C. Certain applications require nuclides with longer half-lives, such as ^{76}Br and ^{52}Fe. In radionuclide therapy positron emitting analogues of therapeutic nuclides, such as ^{110m}In, or daughter nuclides, such as ^{134}La, can enable the use of PET in radionuclide therapy dosimetry. A challenge associated with the use of these positron-emitting nuclides is that they emit gamma radiation in cascade with positrons, which complicates quantitative PET imaging. Other possible complications are the high energies of the emitted positrons, and the decay of ^{52}Fe to the short-lived positron emitter ^{52m}Mn.
Performance measurements were done to investigate the effects of these decay characteristics on the quantitative accuracy, spatial resolution, and other parameters of PET. The distribution of gamma radiation coincidences in PET data was studied and correction methods were implemented and evaluated. PET resolution degrades with 1-2 mm for the studied nuclides in comparison with ^{18}F. The implemented sinogram tail fit and delayed coincidence sinogram based correction methods for cascade gamma coincidences lead to a quantitative accuracy similar as for ^{18}F. Standard dead time corrections are not accurate for these nuclides. Noise equivalent count rates are considerably lower for ^{76}Br than for ^{18}F at clinically relevant radioactivity concentrations.
A method to correct ^{52}Fe patient data for the contribution of the decay daughter ^{52m}Mn is discussed. The use of ^{110m}In is evaluated in a patient study and compared to SPECT imaging with ^{111}In. A dosimetric and PET evaluation of the of use ^{134}Ce/^{134}La for radionuclide therapy and dosimetry is presented. Dosimetry of ^{76}Br-labelled antibodies is evaluated in an animal study. Finally, the possibility to use PET for dosimetry during radionuclide therapy is studied and a dose image calculation program, based on PET measurements, is presented.

Key words: PET, positron emission tomography, quantitative imaging, performance, corrections, bromine, indium, iron, lanthanum.

Mark Lubberink, Uppsala University, Department of Oncology, Radiology and Clinical Immunology, Section of Biomedical Radiation Sciences, Rudbeck Laboratory, SE-751 85 Uppsala, Sweden.

ISSN 0282-7476
ISBN 91-554-5015-6
Printed in Sweden by Eklundshofs Grafiska AB, Uppsala 2001

to Sara

"The giants of science spend their days and nights
Not with wives, not with lovers but searchin' for the lights"

Bruce Springsteen

List of publications

This dissertation is based on the following papers, referred to in the text by their Roman numerals I-VI:

I Lubberink M, Lundqvist H, Westlin JE, Tolmachev V, Schneider H, Lövqvist A, Sundin A, and Carlsson J
Positron Emission Tomography and radioimmunotargeting - Aspects of Quantification and Dosimetry
Acta Oncol **38** 343-349, 1999

II Lövqvist A, Lundqvist H, Lubberink M, Tolmachev V, Carlsson J, and Sundin A
Kinetics of ^{76}Br-labeled anti-CEA antibodies in pigs; Aspects of dosimetry and PET imaging properties
Med Phys **26** 249-258, 1999

III Lubberink M, Tolmachev V, Widström C, Lundqvist H, Bruskin A, and Westlin JE
Evaluation of ^{110m}In-DTPA-D-Phe^{1}-octreotide and Positron Emission Tomography for imaging of neuroendocrine tumours
Submitted to *J Nucl Med*

IV Lubberink M, Tolmachev V, Beshara S, and Lundqvist H
Quantification aspects of patients studies with ^{52}Fe in positron emission tomography
Appl Rad Isot **51** 707-715, 1999

V Lubberink M, Schneider H, Bergström M, and Lundqvist H
Performance evaluation and correction for gamma radiation of ^{76}Br in 2D and 3D PET
Submitted to *Phys Med Biol*; revised version.

VI Lubberink M, Lundqvist H, and Tolmachev V
Production, PET performance and dosimetric considerations of ^{134}Ce/^{134}La, an Auger-electron and positron emitting generator for radionuclide therapy
Submitted to *Phys Med Biol*

Reprints were made with permission from Taylor & Francis (I), the American Association of Physicists in Medicine (II), and Elsevier Science (IV). Institute of Physics Latex style files were used with permission (V, VI).

Front cover (full version only): first PET image of ^{134}La.

Related publications and conference abstracts:

Beshara S, Lundqvist H, Sundin J, Lubberink M, Tolmachev V, Valind S, Antoni G, Långström B, and Danielson BG
Kinetic analysis of ^{52}Fe-labelled iron(III) hydroxide-sucrose complex following bolus administration using positron emission tomography
Br J Haematol **104** 288-295, 1999

Beshara S, Lundqvist H, Sundin J, Lubberink M, Tolmachev V, Valind S, Antoni G, Långström B, and Danielson BG
Pharmacokinetics and red cell utilization of iron(III) hydroxide-sucrose complex in anaemic patients: a study using positron emission tomography
Br J Haematol **104** 296-302, 1999

Lubberink M, Janssen F, Schneider H, Bergström M, and Lundqvist H
Correction for gamma radiation from non-pure positron emitters in Positron Emission Tomography
Presented at Future directions in nuclear medicine physics and engineering, The University of Chicago, Chicago, March 1999

Lubberink M, Widström C, Tolmachev V, Westlin JE, and Lundqvist H
PET and SPECT for indium-octreotide based diagnostics and nuclide therapy dosimetry
Presented at the 46th Annual Meeting of the Society of Nuclear Medicine, Los Angeles, June 1999 *J Nucl Med* **40** 220P, 1999

Lubberink M, Schneider H, Bergström M, and Lundqvist H
Performance evaluation of ^{76}Br in 3D-PET
Presented at the Annual Congress of the European Association of Nuclear Medicine, Paris, September 2000 *Eur J Nucl Med* **27** 1001, 2000

Lundqvist H, Lubberink M, Tolmachev V, Lövqist A, Sundin A, Beshara S, Bruskin A, Carlsson J, and Westlin JE
Positron Emission Tomography and radioimmunotargeting - general aspects
Acta Oncol **38** 335-341, 1999

Preface and acknowledgement

For the last four years, I have been doing this work at the Section of Biomedical Radiation Sciences and at Uppsala University PET Centre. I've had a great, interesting time and I want to thank everybody at BMS and PET for this. There are a number of people that I want to mention especially:

My supervisor, professor Hans Lundqvist, for introducing me to PET and for all his help and ideas during the past years.
This reminds me of the time we were watching a football match and drinking beer at a kebab house in Archamps in 1998, with some French and German graduate students, who were very impressed that supervisors exist that watch football and drink beer with their students, and have a first name other than doctor or professor, which was a surprise for me too when I came to Sweden by the way, and before I forget it, I should also thank him for trying to teach me to write sentences that are less than seven lines long.

Harald Schneider, my other supervisor, for his help with PET and for providing me with inside information on how these PET things actually work (or don't work).

Vladimir Tolmachev, for all the late nights and early mornings producing radioactivity for me, for all his inspiring ideas, and for explaining me about the red and white coffee in Paris.

Professor Bengt Långström for giving me the possibilities to work with the PET cameras, and for the great experience of going to the USA for some PET shopping.

Professor Jörgen Carlsson for his enthusiasm and humour, which set the standard for the atmosphere at BMS.

My co-authors, in no particular order, Alexander Bruskin, Anders Sundin, Anna Lövqvist, Charles Widström, Frank Janssen, Jan-Erik Westlin, Mats Bergström and Soheir Beshara, for stimulating collaboration.

Kalle Fasth and Ulrika Yngwe for getting me bromine every now and then, and the staff at The Svedberg Laboratory for their part in the production of radionuclides.

Rita, Lasse, Karin and Mimmi, for pretending (well, sometimes at least) that I was not in the way, Sasha for programming help, and Tommy and Agneta for making those beautiful phantoms.

Our animal PET work didn't really fit into this thesis, but I should mention Tsuyoshi Kosugi and the others at Hamamatsu Photonics for a good time in Japan, Kayo for the tour of Kyoto, Manon for the 3D measurements, and everybody else at the preclinical lab for the good atmosphere.

Robert and Paco, for proof-reading this thesis, Steve Scott-Robson for language correction of the papers, and Gunnar Blomqvist for helpful comments. I think at least one sentence above would not have passed their judgement.

My friends and colleagues at BMS: Erik, Johanna, and Anna O, for many evenings around a bottle of Starka, and Anna S for sharing the stress of the past weeks with me. Nina, Torbjörn and Shirin for not having lab coats either, Peter for forcing me out for lunch each day, 'the girls next door' for laughing through the wall, Lars for being 'assistent-datoransvarig' when it came to those silly Macs, and everybody for almost never talking work during lunch and coffee breaks. And of course Veronika, Ulla, Agneta, and Maria, for keeping the place organised.

My friends in Uppsala, including everyone I met during my first year as an exchange student, for great fun. My friends in Holland, for, apparently, still being my friends after all my last-minute announcements of the need of sleeping places and catching up on proper beer intake and almost total negligence in the months between those announcements.

And finally my warmest thanks to my parents for their care and support, to my little brother Bart, and to Sara for her patience. I missed you too, and I'll make it up to you!

Uppsala, April 2001

Mark Lubberink

Contents

Abbreviations

BGO	Bismuth Germanate Oxide
CEA	Carcinoembryonic Antigen
CSR	Cold Spot Recovery
DC	Delayed sinogram based gamma coincidence correction
DOI	Depth of Interaction
DTPA	Diethylenetriaminepentaacetic acid
EGF	Epidermal Growth Factor
FBP	Filtered Backprojection
FDG	2-Fluoro-2-deoxy-D-glucose
FOV	Field of View
FWHM	Full Width at Half Maximum
FWTM	Full Width at Tenth Maximum
GSO	Gadolinium Orthosilicate
HSR	Hot Spot Recovery
IEC	International Electrotechnical Commission
LC	Linear tail fit gamma coincidence correction
LOR	Line of Response
LSO	Lutetium Oxyorthosilicate
MAb	Monoclonal Antibody
MIRD	Medical Internal Radiation Dose
NEMA	National Electronics Manufacturers Association
NU+	Maximum nonuniformity
NU-	Minimum nonuniformity
PE	Polythene
PET	Positron Emission Tomography
PM	Photo Multiplier
PSF	Point Spread Function
RC	Recovery Coefficient
ROI	Region of Interest
SD	Standard Deviation
SNM	Society of Nuclear Medicine
SPECT	Single Photon Emission Computed Tomography
SUV	Standard Uptake Value
VOI	Volume of Interest

Colour illustrations

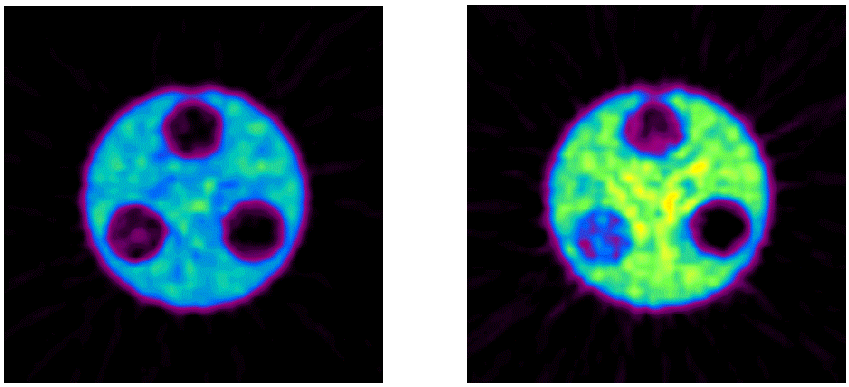

Figure 1: *HR+ images of the NEMA phantom, with water (top), air (right) and Teflon (left) inserts, filled with* ^{18}F *(left) and* ^{76}Br *(right), acquired in 3D mode. Colour scales are similar.*

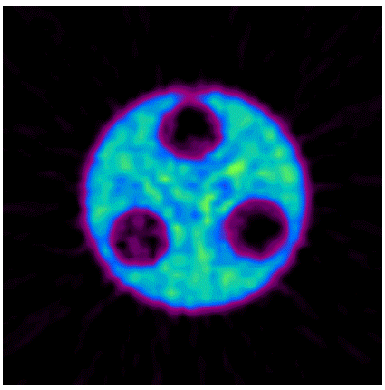

Figure 2: *HR+ image of the NEMA phantom, filled with* ^{76}Br*, acquired in 3D mode. The colour scales are similar as in figure 1. The* ^{76}Br *data was corrected for gamma radiation coincidences by a linear tail fit subtraction.*

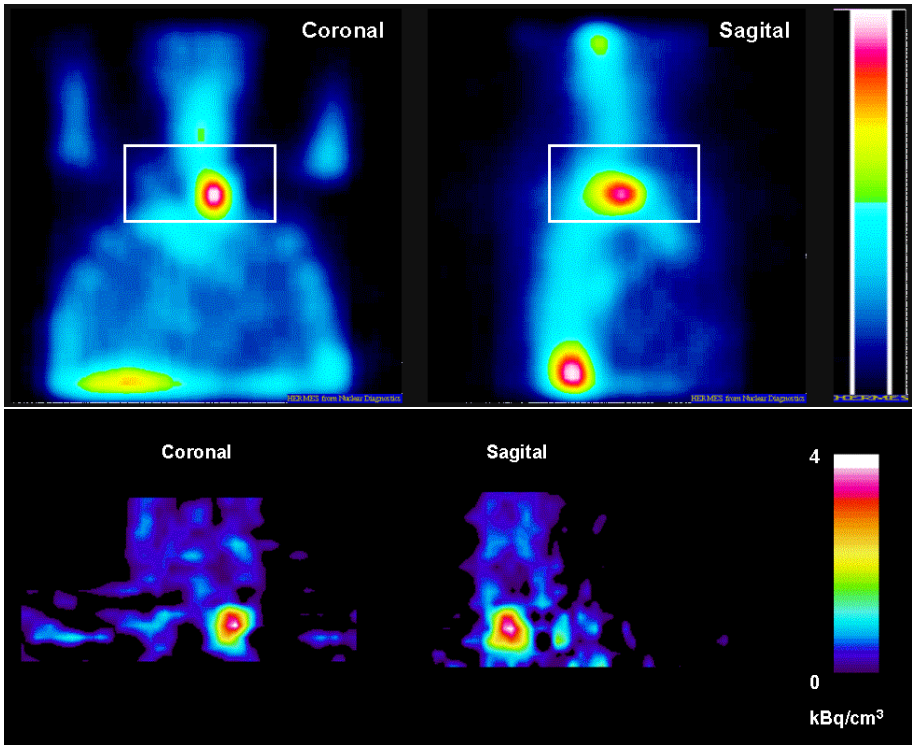

Figure 3: *Top: reoriented SPECT images, 24 h after administration of 175 MBq of* ^{111}*In-octreotide. The rectangles in the images indicate the position of the PET images. Bottom: PET images of the same patient, 1.5 h after administration of 140 MBq* ^{110m}*In-octreotide.*

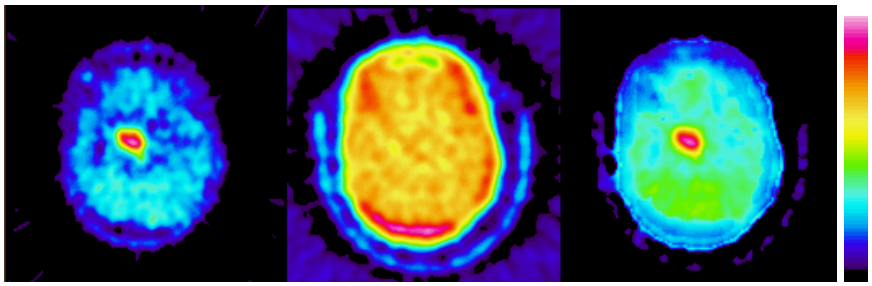

Figure 4: *Radioactivity concentration, attenuation and absorbed dose images of* ^{11}*C-methionine.*

1. Introduction

The potential of annihilation coincidence detection in medical imaging was recognized in the early 1950s [147]. The Anger camera, introduced in 1954, was soon applied for coincidence measurements of positron emitters [9]. However, it was not until the introduction of tomography in the early 1970s that an important step forward was made. Today, positron emission tomography (PET) can visualise and quantify *in vivo* radioactivity distribution with a volumetric resolution below 100 μl and a time resolution of a few seconds.

Usually, PET is associated with the positron-emitting isotopes ^{18}F, ^{15}O or ^{11}C, with radioactive half-lives of about 2 h, 2 min and 20 min, respectively. The last two of these three nuclides require the presence of an in-house cyclotron for nuclide production because of their short half-lives. Mainly ^{18}F has found large-scale clinical application in the form of ^{18}F-fluorodeoxyglucose (FDG), because of its high uptake in areas with elevated glucose metabolism and consequently its effectivity in detecting tumour tissue. Because of its half-life, ^{18}F can be feasibly transported within a radius of a few hundred kilometers.

The availability of positron-emitting nuclides with longer half-lives could expand the possibilities of PET considerably. Furthermore, specific applications, such as studies of the kinetics of antibodies for cancer diagnosis and therapy, require the use of longer-lived nuclides such as ^{124}I or ^{76}Br. An argument for the use of the positron emitters like ^{124}I, ^{86}Y, ^{110m}In and ^{83}Sr is that these are analogues of nuclides used in systemic radionuclide therapy. For example, monoclonal antibodies labelled with ^{124}I will have exactly the same kinetics as when labelled with the therapeutic nuclide ^{131}I. This enables accurate quantification of uptake in tumour and healthy organs using PET. Another nuclide with a very specific application is ^{52}Fe, which can be used to quantify iron-uptake in anaemia patients.

A number of challenges exist when using these nuclides in PET. Firstly, all of these nuclides emit gamma radiation in cascade with positrons in their decays. Secondly, especially ^{76}Br emits relatively high energy positrons, which can travel a distance of almost 2 cm in normal tissue before their annihilation, compared to 3 mm for positrons emitted by ^{18}F. This may affect the spatial resolution. And finally, ^{52}Fe decays to the short-lived positron emitter ^{52m}Mn, so PET studies with ^{52}Fe will result in images that show the sum of ^{52}Fe and ^{52m}Mn radioactivity

distributions.

Aim

The aim of the work presented in this thesis is:

- to evaluate and improve the performance of positron emission tomography with ^{76}Br, ^{52}Fe, ^{134}La and ^{110m}In [I-VI],
- to investigate the performance of ^{110m}In-PET in comparison with ^{111}In-SPECT and to study the possibility of the use of ^{110m}In-DTPA-D-Phe^{1}-octreotide for imaging of neuroendocrine tumours [III],
- to investigate the possibility to quantify the distribution of ^{52}Fe *in vivo* with PET by correcting for the contribution from its positron-emitting daughter ^{52m}Mn [IV],
- to evaluate dosimetric aspects of the use of ^{134}Ce/^{134}La for radionuclide therapy [VI],
- to study the possibility of using PET for radionuclide dosimetry [I,II,VI]

Outline

In chapter 2, the principle of PET will be discussed. Also, the decay properties and previous uses of the radionuclides of interest for this work are discussed and an introduction to their use in radionuclide therapy dosimetry is given. Chapter 3 discusses some experimental aspects, and chapter 4 reports the work done on the effect of the gamma radiation emitted by the nuclides of interest [V]. Chapter 5 discusses resolution and recovery measurements [I-VI]. In chapter 6, applications of ^{52}Fe and ^{110m}In in pharmacological studies and in diagnosis and therapy of neuroendocrine tumours and pharmacological studies, respectively, are discussed [III,IV]. Chapter 6 also considers the application of PET for radionuclide dosimetry [I,II,VI].

2. Background

2.1 Positron emission tomography

2.1.1 Principle

PET is based on the principle of annihilation coincidence detection [110]. Radionuclides administered to a patient emit positrons, that travel a distance of a few millimeters in tissue before annihilation. In this annihilation, two 511-keV photons are simultaneously emitted in opposite directions. If these photons are detected on opposite sides of the body within a very short time, the line along which the annihilation occurred is known (figure 2.1). By surrounding the patient with many detectors, annihilation photons emitted in a large volume and in many angles can be detected (figure 2.2). In this way, the spatial and temporal distribution of molecules labelled with positron-emitting nuclides can be followed *in vivo*.

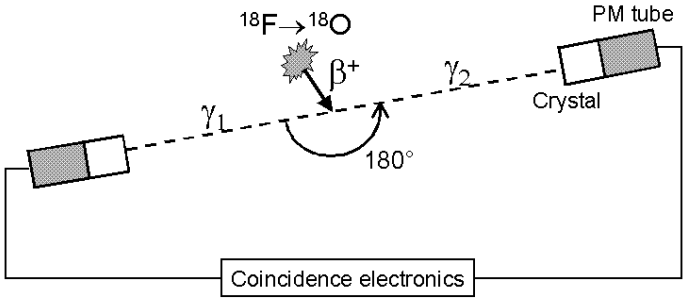

Figure 2.1: *Principle of PET, annihilation coincidence detection.*

2.1.2 Tomographs

Basically, two types of PET systems can be distinguished: those consisting of a few large position-sensitive detectors, and those consisting of rings of large

numbers of small detectors.

Planar detector systems

The earliest PET scanners were made of two opposing Anger cameras ([9]) with 25 mm thick sodium-iodide (NaI) crystals, coupled in coincidence [98]. Later, PET systems were developed consisting of six planar NaI detectors in a hexagonal configuration [69, 99]. Lately, rotating dual-head NaI systems have become more popular again, because of their low cost and large axial field of view (FOV) [82], but the thinner NaI detectors of these systems, optimised for gamma radiation of ^{99m}Tc, are less suitable for PET measurements [65]. Recently, a ring shaped NaI PET system has been developed, consisting of six curved positron-sensitive NaI detectors. This system combines relatively low cost with better sensitivity than dual-headed systems [114].

Block detector systems

Early ring detector systems were built of individual crystals of NaI [110], or later bismuth germanate oxide (BGO) [83], each coupled to a photomultiplier (PM) tube, and coupled in coincidence with a number of detectors on the opposite side of the ring. BGO has a much higher efficiency for detection of 511 keV photons than NaI because of its higher density and atomic number, but it has a lower light output and is not suitable for large planar detectors.

The need of smaller crystals for improved resolution, difficult in a one-to-one crystal-PM tube configuration because of the size of PM-tubes, lead to another configuration. Typical modern ring PET systems [22, 39] contain rings of BGO blocks, cut into 4x4 or 8x8 crystals. Each block read out by four PM tubes using Anger logic for individual crystal identification. These rings of blocks then consists of 4 to 8 detector rings. Systems with crystals individually coupled to PMTs, but also block detector systems, allow higher count rates than planar position-sensitive detector systems. The coincidence time window is limited by the time needed by the annihilation photons to reach the detectors, the light decay time of the detector crystal and the speed of PM tube and electronics, and is normally set around 10 to 20 ns. To reduce the cost of the expensive full ring systems, rotating partial ring systems have also been developed [140].

For brain studies a spherical system has been suggested, giving better sensitivity [43]. A new development is the use of faster crystals with a higher light output than BGO, such as lutetium oxyorthosilicate (LSO) [28] or gadolinium orthosilicate (GSO). A high-resolution brain PET, based on individual GSO crystals coupled to a continuous light guide and an array of photomultiplier tubes, is currently under development [67].

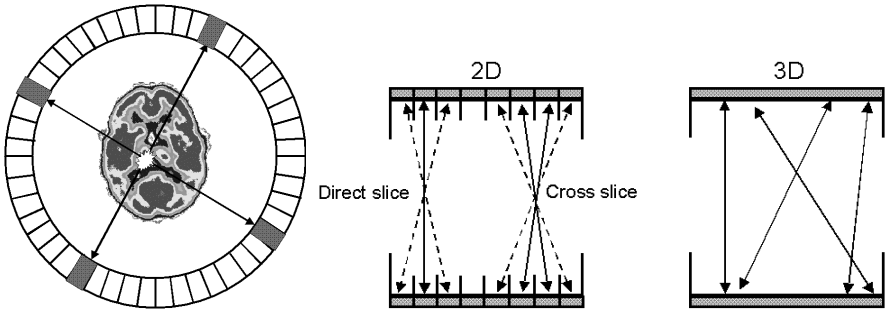

Figure 2.2: *Left: a ring detector system, with two lines of response (LORs) indicated. Right: comparison of 2D and 3D PET. In 2D PET, only coincidences within one ring (direct slices) or neighbouring rings (cross slices) are measured. In systems with small ring dimensions in axial direction, the dashed LORs are added to obtain better sensitivity. In 3D PET, septa are removed and all possible LORs are measured.*

Data acquisition

Each pair of detectors defines a line of response (LOR), or detector channel. Coincidences are usually stored in parallel projections, consisting of coincidences in all LORs at a certain angle through the object. All parallel projections in one ring combination are grouped into a sinogram which can be displayed as a pseudo-colour plot with detector position on the x-axis and LOR angle on the y-axis. List mode acquisition is an alternative form of acquisition where for each coincidence for example time, detector numbers, photon energy etc can be stored, is also possible. This allows for reorganisation of the data in any desired way after the acquisition is completed, but the amount of data and the computation times tend to be large. An overview of PET data acquisition was made by Townsend and Defrise [139].

2D-PET and 3D-PET

Earlier ring PET systems were built with several millimeter thick and up to 20 cm long lead or tungsten septa between the detector rings. These septa were applied to limit the acceptance of coincidences to a two-dimensional geometry (see figure 2.2), accepting only coincidences with one detector ring or between neighbouring rings. They also reduced the possibility of detection of scattered radiation or random coincidences originating from within or outside the detector ring volume. This geometry, now referred to as 2D-PET, leads to small scatter fractions, but the limitation of detection angles also leads to a low sensitivity. In modern PET systems, the septa can be retracted [22, 39], or are not present at all [11, 12, 114]. This geometry is referred to as 3D-PET. Acceptance of coincidences between all detectors rings gives increasing sensitivity, but also leads

to new challenges concerning quantitative measurements, as discussed below [13].

2.1.3 Corrections

The measured sinogram contains all measured coincidences, called prompts. The prompts rate is the sum of the gross trues rate and the random or delayed coincidence rate. The gross trues rate consists of true coincidences, scattered coincidences, and coincidences involving gamma radiation if present in the decay (figure 2.3). A number of corrections have to be performed on the raw data to obtain a sinogram that can be reconstructed to a quantitative image. Below, the necessary corrections are discussed in the order in which they are applied. Correction for gamma radiation coincidences will be discussed in Chapter 4 (paper V).

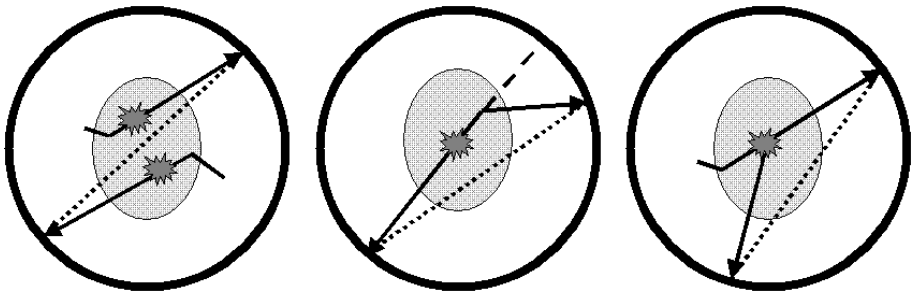

Figure 2.3: *Random coincidences, scatter coincidences and gamma radiation coincidences, from left to right. Solid arrows indicate annihilation photons or gamma radiation, dashed lines indicate the LOR in which a true event should be detected and dotted lines indicate the LOR in which the event is detected.*

Random coincidences

Random coincidences involve two annihilation photons, or gammas, from different decays. Data can be corrected for random coincidences either by subtraction of coincidences measured in a delayed coincidence window, or by calculation of the random coincidence rate in each detector pair using the singles count rates in each detector.

Dead time

Dead time losses are due to front-end detector dead time, caused by the finite light decay time of the scintillation crystal and by the energy discrimination system, as well as the coincidence dead time in the electronics [50, 72, 122, 150]. Usually a measured correction is used to correct for count losses due to dead time. A dead

time curve is determined from a series of measurements of a uniform phantom starting at a high radioactivity concentration and finishing when dead time losses are negligible. The dead time correction is an estimation of the relationship between the dead time and the measured count rate.

Normalisation and arc correction

Normalisation is necessary to correct for the variations in detector and LOR efficiency. Lines of response at the edge of projections have a lower sensitivity than LORs in the centre of a projection and crystals central in a detector block have a better efficiency than crystals at the edge of a block [29]. Arc correction stretches the tails of projections to correct for the difference in effective detector size between the centre and edges of projections, caused by the circular shape of the detector rings [23].

Correction for scattered radiation

Data has to be corrected for coincidences where one or both of the photons have undergone scattering in the object, gantry or detectors. Coincidences for which one or both of the photons have scattered give rise to a scatter fraction of about 10-15% of all measured true coincidences in 2D-PET. Due to the removal of the septa, this fraction increases to about 35% in 3D-PET.

In 2D-PET convolution subtraction methods are often used [14] to correct for scattered radiation. The scatter contribution to each projection element from the other projection elements is described by an analytical function determined by line source measurements. Similar methods have also been suggested for 3D-PET [10, 126], but with limited success because convolution subtraction methods require that the scatter distribution is independent of the source position in the projection direction, which may not always be fulfilled in 3D-PET. Another complication is that the number of prompts should be much larger than the number of LORs to allow for accurate analytical scatter correction methods. This is often not the case in 3D-PET measurements. Dual-energy window scatter correction methods use simultaneous acquisition of data in two energy windows to predict the scatter contamination [1, 54]. An advantage of these "measured" scatter correction methods is that they can account for scatter originating from outside the FOV of the scanner. This is also the case for scatter correction methods based on subtraction of a fit to the projection data outside the object [130]. Another type of 3D scatter correction methods use model-based estimations of the scatter [102, 142], applying Monte-Carlo methods where the uncorrected image is used as an estimate of the radioactivity distribution and the attenuation image represents the scatter medium.

Attenuation

On their way through the body, many photons are scattered or lost and the photon pair is thus not detected in the LOR of its original direction. After 7 cm, 50% of all photons have been scattered in normal tissue. Attenuation correction is usually based on a transmission measurement with a rotating $^{68}Ge/^{68}Ga$ pin source before administration of radioactivity. Other methods are based on contour finding in the emission scan or ellipse definition followed by analytical calculation of the attenuation correction. To decrease noise in the attenuation data, segmentation of the attenuation map can be performed (e.g. [149]). In 3D-PET, transmission scans have to be performed using much weaker pin sources to keep the dead time within acceptable limits. This problem could be overcome by not using the detectors nearest to the transmission source, but in this case a point source with known position has to be used to determine the origin of detected photons [25].

2.1.4 Image reconstruction

Basically, two types of reconstruction methods can be identified: analytical techniques and iterative techniques [139]. Two-dimensional filtered backprojection (FBP), the most common reconstruction method, is based on the central section theorem which states that the Fourier transform of a parallel projection of a 2D distribution, at a certain angle, is equal to the data along a line crossing the origin of the 2D Fourier transform of this distribution at the same angle. Since the sampling of the 2D transform is much denser in the centre than at the edges, the algorithm includes filtering of the Fourier-transformed projections with a ramp filter, often combined with a low pass filter to reduce noise. Three-dimensional filtered backprojection is more difficult because the 3D-PET data set is incomplete. The reprojection algorithm by Kinahan and Rogers [70], for example, uses an image estimate calculated from the straight projection data to obtain the missing line integrals and projections by forward projection, followed by 3D FBP. Other methods apply approximating Fourier rebinning or exact rebinning to reduce the 3D data set to a 2D data set, followed by 2D FBP [38], which greatly speeds up image reconstruction.

In iterative reconstruction techniques [139], projections are calculated from a first estimate of the radioactivity distribution. The calculated projections are compared to the measured projections, and the differences are used to modify the radioactivity distribution estimate. This procedure is repeated until a certain likelihood criterion is met. In general, iterative methods produce images with less noise than analytical methods. This is especially so when the number of counts is of the same order or lower than the number of lines of response. Another aspect of iterative reconstruction methods is that physical aspects of the measurement can be included in the reconstruction.

2.2 Radionuclide therapy and dosimetry

2.2.1 Radionuclide therapy

More than half of all cancer patients can today be cured by surgery, chemotherapy or external radiation therapy. Inoperable tumours or spread disease are still a major challenge. Targeted radionuclide therapy, where a radioactive molecule is taken up specifically in tumour cells, may be of help especially to treat spread disease. Examples of targeting molecules are antibodies, as in radioimmunotherapy, or receptor specific peptides like epidermal growth factor (EGF) or analogues of somatostatin.

A review of nuclides suitable for radionuclide therapy was published by Zweit [153]. A careful selection of radionuclides is important for the success of radionuclide therapy and is much related to the size of the targeted tumours [145, 146]. Nuclides that emit high or medium energy beta particles, such as ^{90}Y and ^{131}I, are useful for treatment of large tumours where the long range of the beta particle can compensate for poor tumour penetration and heterogeneity of the expression of the target molecule. If taken up in single spread cells or micrometastases, these nuclides deposit most of their energy outside the target. In this case alpha particles [96] or lower-energy beta particles are preferable. ^{111}In, for example, has been suggested and used for radionuclide therapy based on the very low energy Auger electrons emitted in its decay [37, 44, 94, 95, 97, 134, 141]. Auger electrons are highly cytotoxic if the Auger-emitting nuclide is taken up into the cell nucleus and decays in close vicinity to the DNA. It has been demonstrated that after internalisation of ^{111}In-labelled peptides, a part (about 10%) of the radioactive atoms is taken up into the cell nucleus and bound to the chromatin [62, 111].

Since many cancer patients undergoing radionuclide therapy may both have large metastases, with poor penetration and possible target expression inhomogeneity, as well as spread single cells and micrometastases, it has been suggested that an optimal treatment should include a cocktail of therapeutic nuclides consisting of both high-energy beta emitters, such as ^{90}Y, and Auger-emitters, such as ^{111}In, attached to the same kind of carrier molecules. A possible approach is then to use a generator where mother and daughter nuclides have different decay schemes and the daughter nuclide has a short radioactive half-life. If the targeting molecule, labelled with the mother nuclide, is internalised into the tumour cells, the daughter nuclide may decay inside the same cell. This is a reasonable assumption with for example radiometals, which are believed to be trapped intracellularly [62, 111]. An example of such a generator system is ^{114m}In/^{114}In [136], in which ^{114m}In ($t_{1/2}$=49.5 d) emits Auger electrons, whereas ^{114}In ($t_{1/2}$=72 s) emits high-energy beta particles.

2.2.2 Dosimetry

Accurate dosimetry has been a prerequisite for the success of cancer therapy with external radiation. The absorbed dose to the tumour should be optimised to maximise the possibility of cell killing, whereas the dose to surrounding healthy tissues should be minimised. In radionuclide therapy of thyroid cancer using ^{131}I the most common practice has been to inject a certain amount of radioactivity per m^2 body surface or per kg body weight [131]. This approach fails to account for patient-dependent differences in metabolism and may lead to sub-optimal doses in the tumour or unnecessary large doses to critical organs. In other forms of radionuclide therapy, such as radioimmunotherapy with ^{131}I-labelled antibodies or therapy of neuroendocrine tumours using somatostatin analogues labelled with ^{90}Y or ^{111}In, the administered amount of radioactivity should be based partly on a tumour dose-response relationship but more importantly on an absorbed dose estimate for the dose-limiting organs such as bone marrow or kidney.

In diagnostic nuclear medicine or for radiation protection purposes radiation doses are often calculated based on population-average tabulated values. The inaccuracy of this method becomes very important at high doses where therapeutic response or normal tissue toxicity can occur and more patient-specific absorbed dose calculations become imperative [131, 152].

MIRD formalism

The most commonly used approach for more or less patient-specific dosimetry is based on the MIRD (Medical Internal Radiation Dose) formalism [85]. The MIRD committee of the Society of Nuclear Medicine developed S-value tables, describing absorbed dose to a target organ per decay in each source organ, for a number of radionuclides and anthropomorphic models, such as the "standard man" phantom and a series of age and sex-specific models [31]. Several dose calculation programs based on the MIRD formalism have been reported (e.g. [59, 84, 129]). Mirdose 3 [129] is an example of an easy to use computerised version of the MIRD scheme. In this program, the only required user inputs are the residence time, which is the integral of the time-activity curve divided by the amount of injected radioactivity, for a number of source organs, and the radionuclide for which doses should be calculated. Drawbacks of the use of the MIRD formalism for therapeutic dose calculations are that it implicitly assumes that radioactivity and absorbed doses are uniformly distributed within organs, that tumours can not be included as source or target regions, and that nobody is built exactly like the "standard man".

Recently, MIRD cellular S-values were published [63], which extend the MIRD formalism to cellular and subcellular source and target regions, with cell and nucleus modelled as concentric spheres of various diameters. Also, MIRD pamphlet no. 17 [19] describes S-values at the voxel level, extending the MIRD formalism to arbitrary radioactivity distributions in volume elements of 3 mm or larger in three dimensions.

Patient-specific non-uniform dosimetry

Dose point kernel methods use a series of three dimensional radioactivity distribution images, measured by for example SPECT, to calculate an absorbed dose distribution by convolution with a dose kernel [52, 75, 78, 84, 125]. It is difficult to apply these methods for dose calculations in regions of varying density because of the inherent density dependence of the dose kernel. Another approach is to use a similar series of images as input for a Monte-Carlo simulation to calculate absorbed doses [46, 47, 133]. This has the advantage that variations in tissue density can be included in the calculations. Both dose kernel and Monte-Carlo methods can account for macroscopic non-uniform radioactivity and absorbed dose distributions.

Cellular dosimetry

For short range radiation such as Auger electrons macroscopic dose information is not sufficient. Because of the importance of the intracellular location of the Auger emitter, and even its location inside the cell nucleus, microdosimetric aspects have to be considered to understand the biological effects of these nuclides [131]. Yet, accurate macroscopic absorbed dose information is an important first step towards a more accurate description of the dose-response relationship.

Measurement of radioactivity distribution

In all patient-specific dose calculations, the result is dependent on the quality of the input data. The accuracy of the residence time or the voxel-by-voxel integrated three-dimensional absorbed dose depends heavily on how well the radioactivity distribution is quantified in space and time. Gamma camera imaging can give crude estimates of radioactivity concentrations. Dynamic SPECT can be used as input for dose kernel or Monte-Carlo methods, but quantification is still a problem because of the limited accuracy of attenuation correction methods for SPECT [79]. In case of radionuclide therapy with ^{90}Y, which only emits beta radiation, targeting substances have to be labelled with for example ^{111}In to measure a radioactivity distribution that may not exactly reflect the distribution of the therapeutic compound [143].

A possible improvement of the radioactivity integral determination is the use of PET with positron-emitting analogues of therapeutic nuclides. For example, ^{124}I, ^{86}Y and ^{83}Sr could be used for dosimetry of ^{131}I, ^{90}Y and ^{89}Sr, respectively [34, 45, 57, 79, 89, 105, 118, 120, 121]. This approach requires a sufficiently long half-life of the positron-emitting nuclide to enable measurement of an adequate part of the radioactivity integral of the therapeutic nuclide. In addition to dose-planning prior to therapy, a small known amount of positron-emitting nuclide may be added during therapy to measure the actual absorbed dose using PET since tumour uptake may be dependent on the amount of administered radioactivity. This presumes that the radiation emitted by the therapeutic nuclide does

not disturb the PET measurement, which will be discussed in chapter 6 (paper I) [109].

Another approach could be the use of positron-emitting short-lived daughter nuclides for dosimetry of a therapeutic parent nuclide. Rösch and co-workers [119] suggested the use of the Auger emitting ^{140}Nd ($t_{1/2}$=3.37 d) for radionuclide therapy, with the positron-emitting daughter nuclide ^{140}Pr ($t_{1/2}$=3.39 min, positron abundance 51%, maximum positron energy 2.3 MeV), which can be used to measure kinetics and dosimetry with PET.

2.3 Positron-emitting nuclides

2.3.1 Standard PET nuclides

At the present time the most common PET application is the use of ^{18}F-labelled fluorodeoxyglucose (FDG) for oncology investigations based on the elevated glucose metabolism of tumours compared to normal tissue. Another application of ^{18}F is the use of F^- for bone scanning. ^{11}C can be used to label many organic compounds such as methionine, used for brain tumour investigation. The main use of ^{15}O is in blood flow and activation studies using radioactive water, while ^{13}N is used to label ammonia for perfusion studies in cardiology. ^{68}Ga is easily produced by a generator, but is mostly used for calibration measurements and in transmission pin sources. A recent application of ^{68}Ga is the labelling of octreotide, a somatostatin analogue for which many tumours have an increased number of receptors [127, 151].

^{18}F, ^{11}C, ^{15}O, ^{13}N and ^{68}Ga are essentially pure positron emitters, that is, the only gamma radiation in their decays are the 511-keV photons produced in the annihilation of emitted positrons. Table 2.1 gives their decay properties and figure 2.4 gives the positron energy distributions of these nuclides.

Table 2.1: *Decay properties of standard positron emitters*

	half-life (min)	β^+ abundance (%)	β^+ energy max, mean (keV)
^{18}F	109.8	96.7	634, 243
^{11}C	20.4	99.8	961, 386
^{15}O	2.04	99.9	1732, 735
^{13}N	9.66	99.8	1198, 492
^{68}Ga	67.6	89.1	1899, 740

Data from the NUDAT database [71].

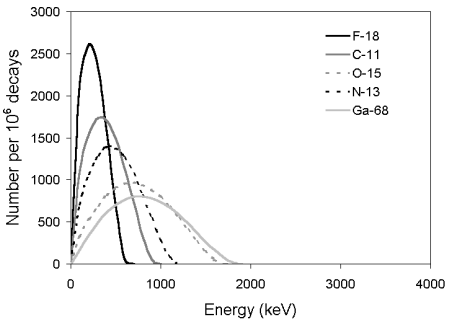

Figure 2.4: *Positron energy distributions of* ^{18}F, ^{11}C *and* ^{68}Ga *[32].*

2.3.2 Bromine-76 [I,II,V]

^{76}Br ($t_{1/2}$ = 16.2 h) has been suggested for labelling of antibodies [87, 88] and of bromodeoxyuridine, a DNA synthesis tracer which has a specific uptake in fast dividing cells such as in tumours [15, 20, 49, 55, 123]. These applications require a nuclide with a half-life longer than any of the standard PET nuclides. The Orsay PET group has developed many ^{76}Br-labelled tracers for *in vivo* mapping of central receptor populations, such as dopamine receptors [92, 93, 104]. Recently the use of ^{76}Br-4-bromodexetimide for imaging of receptors in temporal lobe epilepsy has been reported [41] as well as the labelling of oligonucleotides with ^{76}Br [148].

Apart from positrons (figure 2.5) ^{76}Br emits a large amount of gamma radiation in its decay. The total abundance of gamma radiation with energies over 300 keV, which is the lower PET energy threshold on many scanners, is 198%. In 26% of all ^{76}Br decays, a positron is emitted simultaneously with one 559-keV gamma, and in 22% of the decays a positron is emitted in cascade with more than one gamma among which in most cases the 559 keV gamma. The main decay radiations are listed in table 2.2. Recent publications [112, 113] compared some imaging properties of ^{76}Br and ^{18}F. However, the effect of the gamma radiation emitted in the ^{76}Br decay on image quality was not discussed.

2.3.3 Iron-52/Manganese-52m [I,IV]

Iron metabolism in humans has mainly been studied using the non-positron-emitting isotopes ^{55}Fe and ^{59}Fe [115]. The only iron isotope with suitable decay characteristics for PET, ^{52}Fe, has merely been used as a bone marrow tracer [12, 21, 42]. However, quantitative measurements using PET should also be of advantage in iron uptake studies and in studies of the kinetics of iron-containing

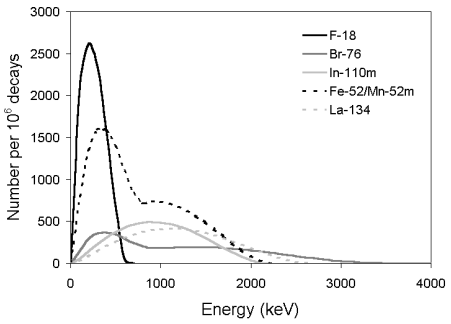

Figure 2.5: *Positron energy distributions of* ^{18}F, ^{76}Br, ^{110m}In, $^{52}Fe/^{52m}Mn$ *and* ^{134}La *[32].*

radiopharmaceuticals. In a study of brain tumour uptake in humans [116] and in studies of iron-sucrose and iron-dextran uptake in both animals and humans [16, 17], the ability to use ^{52}Fe and PET for such studies was demonstrated. In these last studies some measuring problems of technical nature were identified, which were further studied in this work.

The main decay radiation of ^{52}Fe and its decay daughter ^{52m}Mn is given in table 2.2. The positrons emitted in the ^{52m}Mn-decay have relatively high energies (figure 2.5), and apart from positrons also gamma radiation is emitted in the decay. The fact that ^{52m}Mn, produced in the ^{52}Fe decay, is also a positron-emitting isotope raises a special problem in the quantification of ^{52}Fe *in vivo* using PET. Iron and manganese have different kinetics and PET cannot discriminate between ^{52}Fe and ^{52m}Mn. Besides paper IV the only publication known to have addressed this problem is a study by Calonder and co-workers of the kinetics of ^{52}Fe-citrate at the blood-brain barrier of monkeys [27]. They coupled an iron model to a manganese model, based on measurements with pure ^{52m}Mn-citrate, to describe the observed kinetics of ^{52}Fe/^{52m}Mn-citrate.

2.3.4 Indium-110m [I,III]

^{110m}In ($t_{1/2}$ = 69.1 min) also emits many gammas in its decay. The main positron, with an endpoint energy of 2260 keV, is always emitted simultaneously with a 658-keV gamma (see table 2.2 and figure 2.5). The use of ^{110m}In in PET has not previously been reported, but ^{111}In-labelled DTPA-D-Phe^1-octreotide has been used extensively in the diagnosis of neuroendocrine tumours using planar gamma camera imaging and SPECT [77, 101, 103, 135, 144]. Octreotide is an analogue of the neuropeptide somatostatin, receptors for which are overexpressed in many of these tumours. The spatial resolution of SPECT or planar imaging

Table 2.2: *Decay radiation of positron-emitting nuclides in this work*

	half-life	β^+ (max, mean) (keV)	β^+ (%)	$\gamma(keV)$	γ(%)
^{52}Fe	8.28 h	804, 340	55.5	-	-
^{52m}Mn	21.1 min	2633, 1172	98.2	1434	99.8
^{76}Br	16.2 h	3941, 1180	55	559	74.0
				657	15.9
				1216	8.8
				1854	14.7
				2793	5.6
				2951	7.4
^{110m}In	69.1 min	2260, 1038	63	658	98
^{134}La	6.45 min	2688, 1203	62.8	605	5.0

Data from the NUDAT database [71].

limits their capability to detect small tumours [4, 80]. For this reason PET has been suggested as a possible way to improve detection of small lesions [30]. Since octreotide is commercially available in the Octreoscan kit (Mallinckrodt Medical, St. Louis), optimised for labelling with indium, ^{110m}In could be used for labelling of DTPA-D-Phe^1-octreotide. Apart from enabling detection of smaller tumours, ^{110m}In-octreotide-PET can also provide quantitative information about receptor kinetics and concentrations with better temporal and spatial resolution than ^{111}In-octreotide-SPECT.

Another rationale for the use of ^{110m}In in PET is the possibility to improve radionuclide dosimetry of ^{111}In using quantitative ^{110m}In-PET data on the indium-octreotide kinetics during the first hours after administration, in combination with later ^{111}In-SPECT measurements.

2.3.5 Lanthanum-134 [VI]

As mentioned in the previous section, Rösch and co-workers [119] have suggested the generator ^{140}Nd/^{140}Pr for radionuclide therapy. Another generator pair of this kind is ^{134}Ce/^{134}La. ^{134}Ce ($t_{1/2}$ = 3.16 d) emits Auger electrons, and the daughter nuclide ^{134}La ($t_{1/2}$ = 6.45 min) is a positron and Auger-electron emitter (figure 2.5, table 2.2). Both the low-energy Auger electrons emitted in the ^{134}Ce

and ^{134}La decays as well as the high energy positrons emitted in the ^{134}La decay can be considered for radionuclide therapy. The kinetics of the positron-emitting daughter nuclide can be measured with PET and used for dosimetry.

2.3.6 Other nuclides

A number of other positron-emitting nuclides have been used or suggested for PET. A review on the production and use of many of these nuclides was made by Pagani *et al.* [104]. Mainly, ^{124}I has been used for labelling of antibodies [34, 79], which requires a longer half-life than available from the standard PET nuclides, and for dosimetry of ^{131}I radionuclide therapy [34, 45, 79]. PET performance with ^{124}I has been investigated by Pentlow and co-workers [107, 108] with different PET systems, and was found to allow for quantitative measurements. Although it emits more gamma radiation and higher energy positrons ^{120}I may be a shorter-lived alternative to ^{124}I [60, 104]. ^{86}Y has been used for dosimetry of ^{90}Y radionuclide therapy [57, 105, 120, 121] and ^{83}Sr has been suggested for dosimetry of ^{89}Sr radionuclide therapy [89, 120]. Also, ^{66}Ga has been suggested for labelling of antibodies in connection with PET [53]. Three copper isotopes, ^{61}Cu, ^{62}Cu and ^{64}Cu have been suggested for PET. ^{62}Cu has been used as perfusion agent, and can be produced using a ^{62}Zn/^{62}Cu generator system without the need of a local cyclotron. ^{64}Cu-labelled antibodies could be used for dosimetry of radionuclide therapy with ^{67}Cu-labelled antibodies, or could even be used for therapy because ^{64}Cu emits β^+, β^- as well as Auger electrons [104]. ^{64}Cu has also been suggested for labelling of octreotide [5]. ^{61}Cu has physical properties that make it also very interesting for *in vivo* applications, but has not been used as much as ^{62}Cu or ^{64}Cu. Most of these nuclides also emit gamma radiation in cascade with positrons [73, 105]. Table 2.3 and figure 2.6 give some of their decay properties.

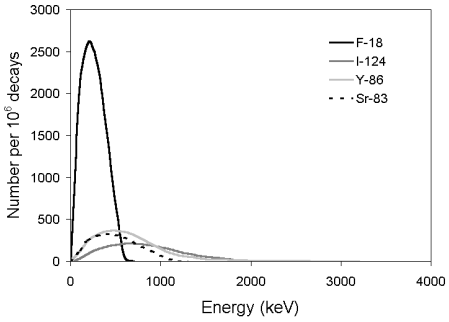

Figure 2.6: *Positron energy distributions of ^{18}F, ^{124}I, ^{86}Y and ^{83}Sr [32].*

Table 2.3: *Decay radiation of other positron-emitting nuclides*

	half-life	β^+ (max, mean) (keV)	β^+ (%)	$\gamma(keV)$	γ(%)
^{61}Cu	3.33 h	1215, 499	61	656	10.8
^{62}Cu	9.67 min	2927, 1314	97.4	-	
^{64}Cu[1]	12.7 h	653, 278	17.4	-	-
^{65}Ga	15.2 min	2179, 887	90	752	8.1
^{66}Ga	9.49 h	4153, 1740	56	884	5.9
				1039	36.9
				2190	5.6
				2752	23.3
^{83}Sr	32.4 h	1234, 496	23	382	14.0
				763	30
^{86}Y	14.7 h	3141, 664	31.9	443	16.9
				628	32.6
				646	9.2
				703	15.4
				777	22.4
				1077	82.5
				1153	30.5
				1854	17.2
				1921	20.8
^{120}I	81.0 min	4378, 1657[2]	78.3[3]	560	73.0
				601	5.8
				641	9.1
				1523	11.2
^{124}I	4.18 d	2138, 819	23.0	603	62.9
				723	10.4
				1691	10.9

Data from the NUDAT database [71].
[1] and β^- 579 keV, 39%
[2] 4593, 1376 [32]
[3] 46% [104], 46%-81% [60]

3. Experimental aspects

3.1 PET systems

Two different types of PET scanners were used in this work: a Scanditronix/GEMS 4096+ 15-WB scanner with non-removable septa (Scanditronix AB, Uppsala, Sweden; General Electric Medical Systems, Milwaukee, Wisconsin) and a CTI/Siemens ECAT Exact HR+ whole body scanner with removable septa (CTI-PET Systems, Knoxville, Tennessee), from here on referred to as "4096" and "HR+". Table 3.1 summarises some properties of both tomographs.

Figure 3.1: *Scanditronix/GEMS 4096+ WB. Photo: Uppsala University PET Centre.*

3.1.1 Scanditronix/GEMS 4096+ 15-WB

The 4096 whole body PET scanner was described in detail by Rota Kops *et al.* [122]. The system produces eight direct planes (coincidences within one detector ring only) and seven cross planes (coincidences between neighbouring rings only). At the front and back of the gantry, 5-cm thick lead rings shield the detectors from external radiation. For blank, transmission and normalisation measurements a

Table 3.1: *Properties of tomographs [22, 122]*

	4096+ WB	ECAT Exact HR+
Number of detectors	4096	18432
Number of rings	8	32
Ring diameter (cm)	101	82.7
Axial FOV (cm)	10.4	15.5
Detectors per block	16	64
Detector size (mm)	6x12x30	4.05x4.39x30
Septa length, thickness	19.5 cm, 3 mm	6.65 cm, 0.8 mm
Energy window (keV)	300 –	350-650
Coincidence windows (ns)	12	12
Intrinsic resolution (mm)	5.8	4.3 (2D), 4.4 (3D)
Sensitivity (cps/Bq/ml)	2.4	5.7 (2D), 27.7 (3D)

rotating ^{68}Ge/^{68}Ga pin source is used. Data is subsequently corrected for random coincidences based on individual detector count rates. Dead time correction is performed according to an analytical function describing the dead time as a function of singles and prompts count rates. After normalisation, scatter correction is done by integral transformation of the projections [14], often referred to as spatially variant convolution subtraction. Transmission data is corrected for scattered radiation using the same method. Finally, attenuation correction is performed either analytically, based on a contour-finding algorithm, or based on a transmission scan. Post-injection transmission scans can be corrected for emission count rates by subtraction of a short emission scan [36]. Images are reconstructed by FBP.

3.1.2 CTI/Siemens ECAT Exact HR+

The ECAT Exact HR+ was described in detail by Brix *et al.* [22]. The number of acquired sinograms is 63 in 2D-mode and 239 in 3D-mode, and 63 image planes are produced. The measurements in the present work were made using the standard settings for data reduction (*mash*, maximum ring difference, and *span*) [22].

For blank and transmission measurements three rotating ^{68}Ge/^{68}Ga pin sources are used. Blank scans and transmission scans are "windowed" [66], that is, only coincidences in the lines of response close to the rod sources are measured, which decreases contamination with scattered events and the contri-

bution of emission counts during a post-injection transmission scan. Randoms are corrected on-line by subtraction of measured coincidence in a delayed coincidence window. Dead time correction is based on singles count rates. Data are subsequently normalised [29] and corrected for geometric accuracy, scatter and attenuation. Scatter correction in 2D mode is made using a stationary convolution subtraction method, while in 3D mode a Monte-Carlo based method is used [142]. Data acquired in 3D was rebinned before reconstruction and all image reconstruction was done using 2D FBP.

Figure 3.2: *Siemens/CTI ECAT Exact HR+. Photo: Uppsala University PET Centre.*

3.2 Production of radionuclides

The production of ^{76}Br, ^{52}Fe and ^{110m}In is presented in papers II, III and IV, and further details can be found elsewhere [90, 137, 138]. Details of the production and the preparation of ^{110m}In-DTPA-D-Phe^{1}-octreotide using the Octreoscan kit from Mallinckrodt are given in paper III. ^{52}Fe-sucrose was produced as described previously [16]. ^{134}Ce was produced using the ^{nat}La(p,xn)^{134}Ce reaction on natural lanthanum at the Gustav Werner Cyclotron (The Svedberg Laboratory, Uppsala, Sweden), as described in paper VI. ^{113m}In (paper I) was produced by the ^{114}Cd(p,2n)^{113m}In reaction using the Scanditronix MC17 cyclotron (Scanditronix, Uppsala, Sweden) at Uppsala University PET Centre.

3.3 Performance measurements

Both the National Electronics Manufacturers Association (NEMA) and the International Electrotechnical Commission (IEC) have established standards for performance measurements of PET scanners [56, 64, 68, 100]. New NEMA guidelines are in preparation [2], which will asses performance parameters more relevant to clinical whole-body imaging situations. These standards were developed to enable more or less objective comparison of different scanners. In this work performance measurements were carried out to compare PET performance of different radionuclides instead of different scanners. Therefore the NEMA or IEC guidelines were slightly modified. The phantoms used in the measurements are shown in figure 3.3.

3.3.1 Spatial resolution [I-VI]

Both NEMA and IEC suggest measurement of transaxial resolution using a steel needle line source in air, parallel to the camera axis, and application of the sharpest possible filter in reconstruction. Transaxial resolution is then calculated as the full width at half maximum (FWHM) and at tenth maximum (FWTM) of the point spread function (PSF) in the image of this line source, determined by linear interpolation between image points. In the rest of this work, "point spread function" will refer to a profile of the image of a line source placed in the tomograph parallel to the axis of the FOV, and not to a profile of the image of an actual point source.

In the measurements described in this work [III,V,VI] the polythene phantom described in figure 3.3C was used and placed on the patient bed. In this phantom the influence of positron range can be measured as the positrons are transported in material close to tissue equivalence and are not absorbed locally as in a steel needle line source. The filters generally used in clinical studies were used: a 4 mm Hann filter on the 4096 and a 4 mm Hann filter or a 6 mm Gaussian filter on the HR+. FWHM and FWTM were determined by linear interpolation and the pixel size was 1.03 mm (HR+) and 2 mm (4096), in the latter case the minimum pixel size required for measured attenuation correction considering the size of the phantom.

In a second measurement [I,II,IV] the phantom shown in figure 3.3D was used. In the reconstruction a 1-mm ramp filter or a 4-mm Hann filter was applied and spatial resolution was determined as above. This measurement was also used to calculate "line source recovery" by analysing the total radioactivity in concentric regions of interest (ROIs) around the centre of PSF, which will not be discussed here.

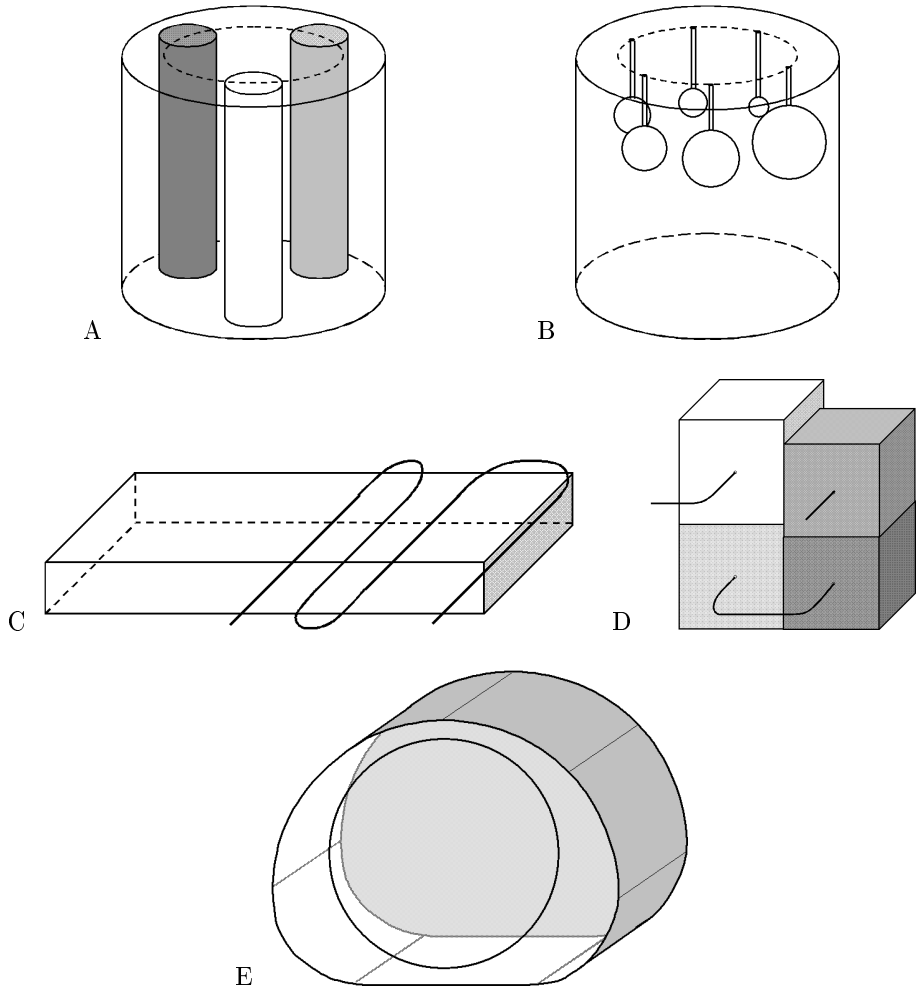

Figure 3.3: *Schematic drawings of performance test phantoms. A. Correction accuracy phantom, 20-cm diameter cylinder with removable 5-cm diameter water, air and teflon inserts at 6 cm from the phantom axis; steel needle line sources can be placed at 0, 4.5 and 9 cm from the phantom axis. B. Recovery phantom, 20-cm diameter cylinder containing fillable glass spheres with diameters ranging from 10 to 38 mm. C. Polythene 45x20x5-cm spatial resolution phantom with a catheter crossing it at 0, 5, 10 and 20 cm from its centre. D. Phantom used to measure density-dependent density in polythene, two types of wood, and bonded foam, with densities of 1.0, 0.5, 0.2 and 0.15 g/cm^3; the dimensions of the blocks are 10x10 cm for the two highest density materials, and 12x12 cm for the two lowest density materials; E. 30x23 cm torso phantom; the circle indicates a lid, which can be replaced with the lid of the sphere phantom B.*

3.3.2 Recovery [III-VI]

Hot spot recovery [III,V,VI]

The NEMA protocol does not include recovery measurements. In the IEC protocol, recovery is measured using a phantom as shown in figure 3.3B. The centres of the spheres should be positioned at different axial positions and both a cross slice and a direct slice should pass through each sphere. The IEC standard requires that the spheres are removed after the measurement and the cylinder is uniformly filled with the same solution as used in the spheres. The data from that measurement should serve as a reference radioactivity concentration [3].

For a complete description of recovery, measurements should be made at different positions in the FOV with differently shaped phantoms, different reconstruction filters, and with different object shapes. In the measurements described here the phantom was positioned on the patient bed with its front at the entrance of the axial FOV so that the spheres were approximately 5 cm from the edge of the FOV. Analytical (HR+) or measured (4096) attenuation correction was applied. All images were reconstructed to a 1.03-mm pixel size. For hot spot recovery (HSR) calculations either one slice through the centre of each sphere was used (HR+) or a cross slice and a direct slice through each sphere were used (4096). To ensure comparable results and to avoid the problem of different ROI calculation methods in different image analysis tools, a computer program was written to determine these ROI concentrations automatically. In each sphere, the program determines the pixel with maximum radioactivity concentration. Then a 50% level ROI is calculated, containing all pixels with a measured radioactivity concentration of 50% or more of the maximum pixel radioactivity concentration in each sphere. From this ROI, the geometrical centre of the sphere is determined and ROIs with diameters equal to the FWHM of the spatial resolution and 1-cm diameter ROIs are calculated, including all pixels with a distance less or equal than the desired radius. Recovery coefficients were related to the measured radioactivity concentration in the resolution size ROI in the largest sphere instead of to the true radioactivity concentration, since it is difficult to prepare solutions with identical radioactivity concentration. The following equation was used:

$$HSR_i = C_i / C_{largest} \tag{3.1}$$

where C_i is the radioactivity concentration either in the maximum pixel, in a 1-cm diameter ROI, in a ROI with diameter similar to the spatial resolution, or in a ROI at 50% of the maximum radioactivity concentration.

Size estimation [V,VI]

The radii of the 50% level ROIs were also compared to the true sphere sizes. This was done to evaluate the accuracy of size estimation using a ROI drawn at 50% of the maximum radioactivity concentration of an object.

Cold spot recovery [V]

The phantom in figure 3.3B was used to measure cold spot recovery (CSR) coefficients. The spheres were filled with non-radioactive water and the rest of the phantom with a radioactive solution. Emission scans were made until 2 $\times 10^9$ gross trues were acquired. Analytical attenuation correction was applied. For calculation of cold-spot recovery coefficients, the mean radioactivity concentration in resolution-sized ROIs in three planes crossing the spheres were divided by the mean of the radioactivity concentration measured in 15-cm diameter ROIs in five image planes not containing the spheres.

3.3.3 Scatter and attenuation correction accuracy [III-VI]

According to the NEMA protocol scatter correction accuracy should be measured using the phantom in figure 3.3A, positioned with its centre 2.5 cm above the camera axis, with only the cold water insert in place and using analytical attenuation correction. Attenuation correction accuracy should be measured using the same phantom with all three inserts in place and the phantom again positioned 2.5 cm off-centre. Correction errors are calculated by dividing the radioactivity concentration in a 3-cm diameter VOI in each insert by the radioactivity concentration in a number of similar VOIs in the radioactive solution.

Since we were not interested in either attenuation or scatter correction per se, but in comparable results between different nuclides, only measurements with all three inserts in place were made. The phantom was placed in the HR+ head support or connected to the end of the 4096 patient bed, and positioned centrally in the FOV. Measured attenuation correction was applied.

3.3.4 Count rate characteristics [V]

Noise equivalent count rate

Noise equivalent count rate (NEC) [132] was calculated from a decay series measurement of a 20-cm diameter uniform cylinder, according to the following equation:

$$NEC = \frac{T^2}{T + S + fG + 2fR} \tag{3.2}$$

Here, T is the net trues rate, S is the scatter rate, calculated as the NEMA scatter fraction for a nuclide emitting only positrons [22] multiplied with the gross trues rate minus the gamma coincidence rate, G is the gamma coincidence rate, determined by a projection tail fit (see chapter 4, paper V), R is the random coincidence rate, and f is the fraction of the sinogram covered by the object. The factor 2 in $2fR$ arises from the noise contribution of delayed coincidence random correction. Instead of using the gamma coincidence fraction fG, the NEMA scatter fraction could be measured for each separate nuclide.

Count rate linearity

Gamma radiation may lead to incorrect dead time corrections. System count rate linearity was studied in a decay measurement as in the previous paragraph. The measured radioactivity concentration in a 15-cm diameter VOI covering the whole axial FOV, after decay and dead time correction, was plotted versus the known radioactivity concentration in the cylinder.

3.3.5 Uniformity [V]

The NEMA standard advises calculation of uniformity by drawing adjacent 1-cm square ROIs in the image of a 20-cm diameter uniform phantom, containing a certain number of true counts. Maximum and minimum non-uniformity were calculated as specified in the NEMA protocol, both within a slice (slice uniformity) and in the entire FOV (volume uniformity), with the exception of the use of 2x2-cm instead of 1x1-cm square ROIs. As a second measure of uniformity the relative standard deviation in a 15-cm diameter VOI covering the whole axial FOV was calculated. Emission scans of 100 million gross true events or approximately 100 million gamma-corrected trues were used. Measurements were made both with a 20-cm diameter uniform cylindrical phantom and with a torso phantom (figure 3.3E).

3.3.6 Radioactivity outside the FOV [V]

In 3D PET, coincidences of scattered radiation and the increased random rate originating from radioactivity outside of the FOV pose a major problem in quantitative PET studies [128]. For example, a large radioactivity concentration in the heart may seriously influence brain measurements. The existing NEMA and IEC standards do not include measurements of the influence of radioactivity outside of the FOV. Here, the relative effect of ^{76}Br compared to ^{18}F outside the FOV was considered using two different measurements. In the first measurement a point source filled with approximately 40 MBq was positioned on the patient bed starting at 50 cm outside the FOV, and moved inward in steps until it was in the centre of the FOV. At each position, a 5-min emission scan was made. In the second measurement, the phantom in figure 3.3A was positioned central in the FOV of the scanner, with the water insert below the phantom axis. The phantom was filled with approximately 40 MBq and 15-min emission scans were made, both with and without a 40 MBq external source positioned on the patient bed at 10 cm from the phantom. Measurements were done both with and without the neuro-insert, a side-shield for brain studies delivered with the HR+ scanner.

3.4 Calibration and radioactivity measurements [I-VI]

For all nuclides, the dose calibrator (Beckman-Coulter, Fullerton, California) used to measure radioactivity before administration and the well-counters used to measure blood samples at Uppsala University PET Centre were cross-calibrated with a solid state detector (EG&G Ortec High Purity Gamma-X Germanium detector, Oak Ridge, Tennessee). This high-purity germanium detector was absolutely calibrated using a ^{157}Eu source (Amersham Pharmacia Biotech, Uppsala, Sweden) with 2% uncertainty in radioactivity. Cross calibration constants between solid state detector, ionisation chamber, well counters and PET camera were determined for each nuclide and for ^{52}Fe/^{52m}Mn in physical equilibrium.

4. Effects of gamma radiation

4.1 Scatter and attenuation correction accuracy [I-VI]

Figure 1 shows two HR+ 3D images of the NEMA phantom (figure 3.3A). In the left image, the phantom is filled with ^{18}F, and in the right image with ^{76}Br, and standard corrections for scatter and attenuation were applied. It is apparent that the corrections are not adequate for the ^{76}Br measurements. Tables 4.1 and 4.2 give measured scatter and attenuation correction accuracy values for different nuclides with the HR+ and 4096 tomographs.

Table 4.1: *Scatter and attenuation correction errors HR+ in 3D mode (%; mean of six scans; ± 1)*

	2D			3D		
	^{18}F	^{76}Br	^{134}La	^{18}F	^{76}Br	^{134}La
Water	8	17	9	8	27	12
Air	10	7	10	2	-4	2
Teflon	9	27	10	16	56	23

The results for ^{18}F show that the scatter and attenuation correction methods of the HR+, both in 2D and in 3D, are sub-optimal compared to the scatter and attenuation correction of the 4096. Note that the HR+ measurements were made with the phantom on the head support, central in the FOV, and with a hot transmission scan for attenuation correction, whereas the 4096 measurements were done with the phantom attached to the end of the patient bed, central in the FOV, and with attenuation correction based on a cold transmission scan. In each

Table 4.2: *Scatter and attenuation correction errors 4096 (%; ±1)*

	^{18}F	^{76}Br	^{110m}In	^{52}Fe/^{52m}Mn
Water	2	5	6[a]	2[b]
Air	8	8	-	-
Teflon	-3	5	-	-

[a] [III], measurement with only water insert
[b] [I, IV], different phantom

case, the transmission measurement consisted of about 10^8 true counts. Results for the HR+ with ^{18}F using a cold transmission scan for attenuation correction were approximately 1% better. The correction accuracy results are consistent with other data [124] but not with the results published by Brix *et al.* [22] which gave correction errors of approximately 0% for ^{18}F in both 2D and 3D modes with this phantom positioned 2.5 cm off-centre .

4.2 Correction for gamma radiation coincidences [V]

4.2.1 Distribution

Figure 4.1 shows projections of a uniform cylinder filled with ^{76}Br or ^{68}Ga. These projections were corrected for random coincidences and to facilitate comparison between ^{76}Br and ^{68}Ga they were scaled by the total number of true and scatter counts measured inside the phantom as determined by subtraction of a background calculated by linear interpolation of the counts just outside the phantom. For uniform cylinders the gamma radiation coincidence fraction measured in this way was 45% of the gross trues counts for the HR+ in 3D mode, 32% for the HR+ in 2D mode, and 12% for the 4096. Projections of the torso phantom (figure 3.3E), also scaled by the number of counts inside the phantom, are shown in figure 4.2.

4.2.2 Correction methods

The background in sinograms from gamma-emitting PET nuclides is very different in shape than a background just caused by scatter. Standard convolution subtraction and model-based scatter correction methods can therefore not be applied directly on the raw data. The aim of a correction for gamma radiation coincidences was to produce sinograms that can be used as input in the standard scatter correction methods. The gamma coincidence correction could then be

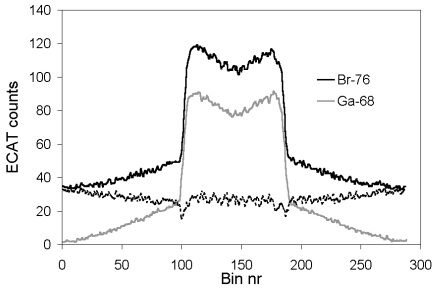

Figure 4.1: *3D projection of a central uniform cylinder filled with ^{76}Br (solid black line) or ^{68}Ga (grey line). The difference between the two projections is indicated.*

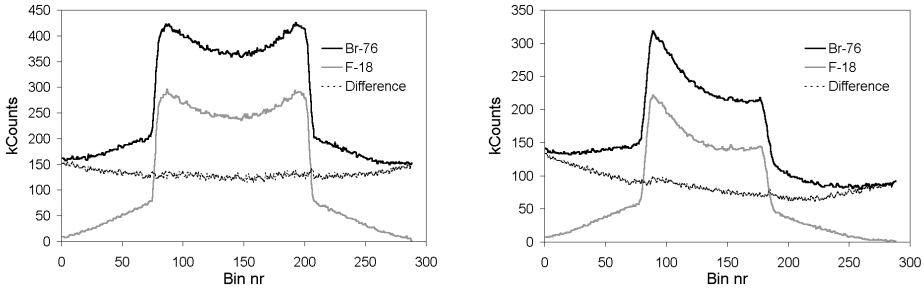

Figure 4.2: *Projections of a torso phantom along the long and short axis of the phantom.*

applied on any system without having to change established scatter correction methods.

Projection tail fitting

Figure 4.1 suggests that subtraction of a uniform background, determined by the mean of the counts in the projection tails, would be sufficient for objects in the centre of the FOV. This was also suggested by Pentlow and co-workers [105, 106] for ^{86}Y, although they suggested a correction after normalisation of the data. Since normalisation leads to much increased values at the projection tails [V], tail fit correction after normalisation will lead to an overestimation of the gamma coincidence contribution in the central part of the projections. A similar approach, which may be more correct for more off-centre distributions

(figure 4.4 left), is the subtraction of a background determined by a linear fit to the counts in the projection tails [73]. Both these corrections were implemented on the 4096 and HR+ scanners. For the HR+, only 90% in 2D and 80% in 3D, of the tail counts were subtracted since the scatter contribution is not zero at the projection tails.

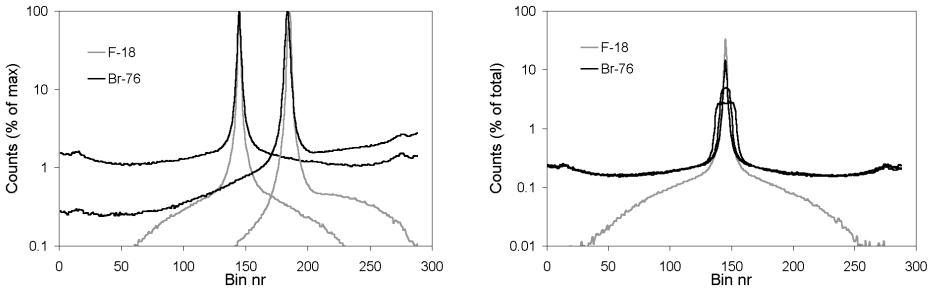

Figure 4.3: *Normalised 2D projections of line sources at different positions inside a 20-cm cylinder, along the line though both phantom axis and line source (right) and perpendicular to this (left).*

Convolution subtraction method

Line source measurements showed that the distribution of cascade-gamma coincidences is approximately shift-invariant along the projection direction in 2D-mode (figure 4.3). Because of this it is in principle possible to implement a spatially variant convolution subtraction type of cascade-gamma coincidence correction. However, so far no satisfactory fit function has been found. Another option is the implementation a of nuclide-specific convolution subtraction method to correct both for scatter and for gamma radiation. In 3D-mode the gamma radiation coincidence distribution is not shift-invariant.

Delayed-coincidence based correction

In figure 4.4 a measured delayed coincidence projection and an estimated gamma coincidence projection for a 10 cm off-centre NEMA phantom are shown. Apparently the shape of the random coincidence sinogram is approximately similar to the shape of a gamma radiation coincidence sinogram. This can be used for gamma coincidence correction by appropriate scaling of the delayed coincidence projections using the count rates in the tails of the emission projections. This correction was tested for the HR+ system.

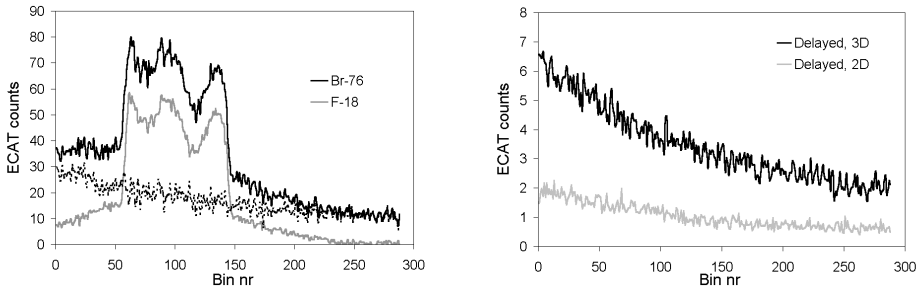

Figure 4.4: *Projections of a 10 cm off-centre NEMA phantom in 3D mode (left) and delayed coincidence projections at the same angle (right) in 3D and 2D mode.*

Table 4.3: Correction errors (%; ± 1) for ^{76}Br in water, air and Teflon, after linear tail fit gamma coincidence correction

	HR+ 2D	HR+ 3D	4096
Water	8	8	1
Air	11	3	9
Teflon	10	15	-6

4.2.3 Correction evaluation

Figure 2 shows NEMA phantom images after correction for gamma radiation coincidences by linear tail fit subtraction. Table 4.3 gives the overall correction accuracy for ^{76}Br after correction for scattered radiation, attenuation correction and correction for gamma radiation coincidences by linear tail fit subtraction, measured using a NEMA phantom central in the FOV. Correction for gamma coincidences based on delayed sinograms after smoothing of the delayed projections with a 1-cm mean filter gave similar results. Overall correction accuracy is approximately similar for ^{76}Br and ^{18}F, both on the HR+ and the 4096 cameras.

A complication with the use of tail fits is the low number of counts in the projection tails in patient studies. Usually in the order of 10-50 MBq of ^{76}Br is administered to limit radiation dose to the patient while scan times are kept relatively short. For the shorter-lived ^{110m}In higher amounts of radioactivity can be administered, so this may be less of a problem. In this case correction based on the delayed coincidence sinogram may be more useful, as may a convolution subtraction method. This should be subject of further investigations. Complica-

tions with the use of the delayed coincidence based correction are that the delayed coincidence projections are noisy which can be decreased to a certain extent by appropriate smoothing, and that detectors near transmission pin source storage locations have higher random rates than other detectors which does not reflect higher gamma coincidence rates.

4.3 Count rate characteristics

4.3.1 Noise equivalent count rate [V]

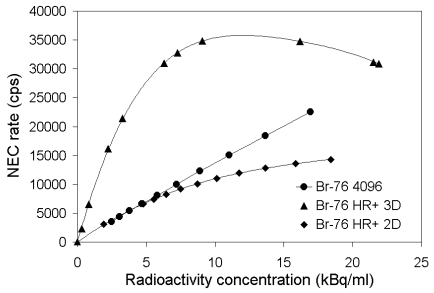

Figure 4.5: *Noise equivalent count rates for ^{76}Br, measured with the 4096 and with the HR+ in 2D and 3D mode.*

Figure 4.5 shows that the ^{76}Br NEC rate at clinically relevant radioactivity concentrations is about 1000-2000 cps in 2D mode and 10000 cps in 3D mode. This is less than one-tenth of the NEC rate of ^{11}C or ^{18}F at relevant concentrations [3]. The ^{76}Br random rate is higher than the net trues rate at any radioactivity concentration in 3D mode. The image signal to noise ratio and the NEC rate may be improved slightly by appropriate filtering of the delayed coincidence projections before random correction and their possible use for gamma coincidence correction.

4.3.2 Count rate linearity [V]

Results of count rate linearity measurements with the 4096 and the HR+ tomographs are shown in figure 4.6. The HR+ dead time correction fails for ^{76}Br both in 2D mode and in 3D mode. The HR+ dead time correction is based on the singles count rate, which underestimates ^{76}Br dead time. The 4096 correction is based on both singles and prompts rates which apparently leads to a correct estimation of the dead time, although absolute radioactivity concentration is overestimated.

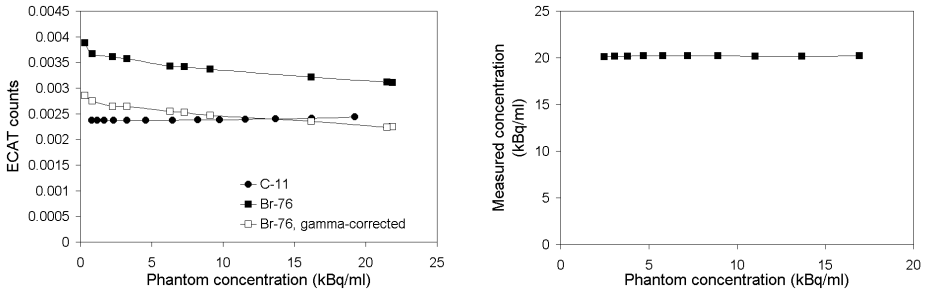

Figure 4.6: *HR+ 3D counts per second per voxel (left) and 4096 measured radioactivity concentration (right) after decay, dead time and abundance correction*

4.3.3 Nuclide-independent count rate model (ongoing work)

The ECAT Exact HR+ uses a dead time correction based on a quadratic fit of the dead time to the singles count rate. As demonstrated above, this correction does not work well for ^{76}Br. A simple system dead time model was used to investigate the possibility of a nuclide-independent dead time correction.

The system count rate behaviour can be described in terms of the measured singles and prompts rates as:

$$T_m = \lambda_S^2(S) \cdot \lambda_C(P) \cdot T_{ex} \tag{4.1}$$

T_m is the measured gross trues count rate, $\lambda_S(S)$ is the singles life time, relative to the measurement time, as a function of the measured singles rate, $\lambda_C(P)$ is the coincidence life time as a function of the measured prompts rate, and T_{ex} is the "ideal" trues count rate as extrapolated from the measured trues count rate at low activity concentration in a decay measurement. Multiple coincidences are registered as separate coincidences between all involved detector pairs, and are neglected in this model. The data from a series of measurements of a cylindrical phantom during several half-lives of a nuclide can be used to determine λ_S:

$$\lambda_S = \frac{S_m}{S_{ex}} \tag{4.2}$$

where S_{ex} is determined by linear extrapolation from the measured singles rates S_m at low radioactivity concentrations. The coincidence life time λ_C can then be calculated as follows:

$$\lambda_C = \frac{T_m}{\lambda_S^2 T_{ex}} \tag{4.3}$$

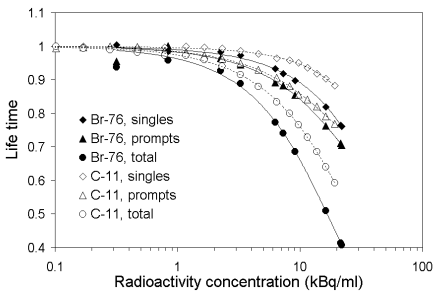

Figure 4.7: *Singles, prompt and total life times as a function of radioactivity concentration.*

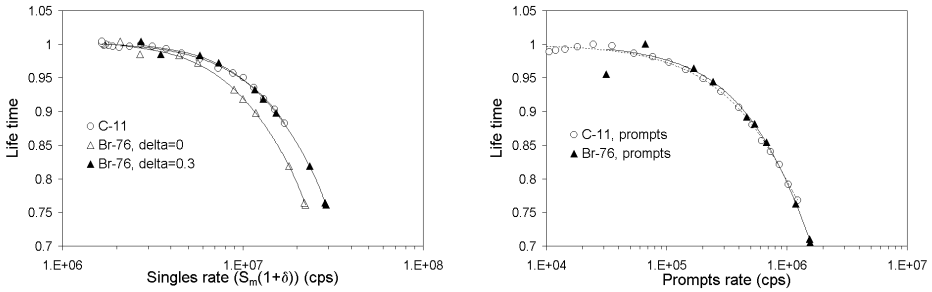

Figure 4.8: *Singles (left) and prompts (right) life times.*

Figure 4.7 shows the life times as a function of radioactivity concentration and figure 4.8 shows the life times as a function of singles and prompts rates. Apparently the singles life time as a function of the singles rate is not the same for ^{76}Br as for ^{18}F. Therefore a singles life time function λ_S, fitted to ^{11}C data, does not predict the ^{76}Br life time accurately.

This problem is caused by the high-energy gamma radiation emitted by ^{76}Br. Gamma radiation with energy outside the camera's energy discrimination window is rejected and not counted in the measured singles count rate. However, these rejected singles do contribute to the detector dead time and this should be accounted for in the calculation of the singles life time factor λ_S. Assuming that the contribution of rejected singles to the detector dead time is equal to the contribution of accepted singles, equation 4.2 should read:

$$\lambda'_S = \frac{S_m(1+\delta)}{S'_{ex}} \tag{4.4}$$

where S'_{ex} is the extrapolated singles rate of $S_m(1+\delta)$. Gamma radiation rejected by the energy discriminator is accounted for by δ, with δ=0 for ^{11}C and δ=0.3 for ^{76}Br (see figure 4.8). Introduction of this factor δ leads to the possibility to use the same singles dead time fit for any nuclide. The dead time corrected trues count rate T_C is then calculated as:

$$T_c = \frac{T_m}{\lambda'^2_S \lambda_C} \tag{4.5}$$

Using equation 4.5, the ^{76}Br dead time is accurately predicted by third degree polynomial dead time functions fitted to the ^{11}C data.

4.4 Uniformity [V]

Tables 4.4 shows maximum and minimum non-uniformity for ^{76}Br and ^{18}F for the HR+ system in 3D mode.

Table 4.4: Slice and volume nonuniformity (%) in a cylindrical phantom for ^{76}Br and ^{18}F. DC = delayed sinogram based gamma correction, LC = linear background subtraction.

	NU+	NU-	VOI SD/mean
^{18}F, slice	3.0	2.2	
^{76}Br, slice	3.4	5.6	
^{76}Br, slice, DC	3.5	5.7	
^{76}Br, slice, LC	4.0	4.5	
^{18}F, volume	15	12	14.2
^{76}Br, volume	23	19	23.6
^{76}Br, volume, DC	21	21	24.6
^{76}Br, volume, LC	17	19	23.6

The images used to calculate ^{76}Br non-uniformity before gamma correction contained 100 million gross true counts, as did the ^{18}F images, whereas the images used to calculate non-uniformity after gamma correction contained 185 million gross true counts, resulting in approximately 100 million counts after gamma correction. These numbers of counts are about similar to those recommended by the IEC protocol, but the NEMA protocol requires acquisition of 20 million counts per slice. Apart from the lower noise equivalent count rates for ^{76}Br than for ^{11}C at similar radioactivity concentrations, the high non-uniformity for uncorrected ^{76}Br images can at least partly be attributed to the lower number

of counts inside the phantom compared to the other images. Apparently the delayed sinogram based gamma radiation correction leads to a slightly higher non-uniformity than the linear projection tail fit correction, and in both cases the non-uniformity is higher than for ^{18}F for a similar number of net trues. In case of delayed sinogram based correction this increase is caused by the noise in the delayed sinogram, an effect that could be reduced by more smoothing of the delayed projections. In case of the linear background subtraction a reason may be the use of the background subtraction before normalisation of the data.

4.5 Radioactivity outside the FOV [V]

Figure 4.9 shows measured trues count rates of a measurement with a point source at various distances to the entrance of the axial FOV. Clearly, count rates are very much increased for ^{76}Br compared to ^{18}F. For a similar trues count rate inside the FOV the trues count rate at 10 cm outside the FOV is ten times higher for ^{76}Br than for ^{18}F and two times higher with use of the neuro-insert.

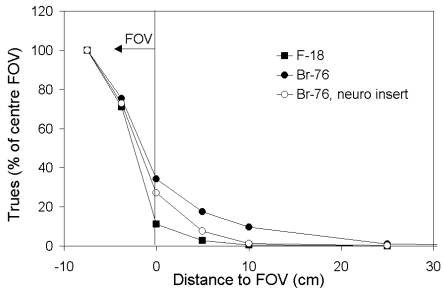

Figure 4.9: *Gross trues count rates from a point source on the patient bed versus the distance to the entrance of the axial FOV, comparing ^{76}Br and ^{18}F with and without neuro-insert.*

Other measurements showed that activity outside the FOV leads to increased measured radioactivity concentrations, especially in slices at the side of the axial FOV furthest from the external source. In the detector rings close to the edge of the FOV at the side of the external source, the detectors do not "see" the source because of the shielding at the edge of the axial FOV. For more remote detector rings, the edge septa do not shield the external source, which results in increased measured radioactivity concentration caused by an increase in scattered radiation and gamma radiation coincidences. Application of gamma coincidence correction seems to remove this effect, but further investigation is necessary.

5. Resolution, recovery and contrast

5.1 Introduction

The spatial resolution of a ring detector system is determined by:

- the non-collinearity of the annihilation photons;
- the positron energy distribution;
- the size of the detectors;
- the uncertainty of the depth at which a photon is detected in the crystal, which is especially important at the edge of the FOV and leads to incorrect LOR assignment (parallax effect);
- intercrystal Compton scatter of annihilation photons and scintillation light multiplexing in block detectors;
- and the reconstruction filter.

The first two effects lead to a physical spatial resolution limit of 2 mm for whole-body scanners [81]. To decrease the parallax effect, caused by the length of the detectors in radial direction, phoswich detectors combining different detector materials with different light decay times can be used to determine the depth of interaction of a photon [35].

Due to the limited spatial resolution of PET small structures of uniform radioactivity concentration are displayed on a larger area and with a blurred radioactivity distribution. This partial volume effect is for example apparent in measurements of blood radioactivity concentrations in the left ventricle of the heart (e.g. [86]) and in measurements of small structures in the brain (e.g. [58]). For accurate quantification partial volume correction, or recovery correction, has to be performed [61].

Spatial resolution, recovery and contrast of ^{76}Br, ^{52}Fe, ^{110m}In and ^{134}La will be discussed in this chapter.

5.2 Transaxial resolution

5.2.1 Transaxial resolution vs. distance to axis [III,V,VI]

Figure 5.1 shows the spatial resolution of the 4096 and HR+ systems in polythene for ^{18}F, ^{76}Br, ^{110m}In, and ^{134}La. Images were reconstructed using a 4 mm Hann filter, the standard clinical filter size for brain studies. There was no significant difference between the 2D and 3D HR+ resolution.

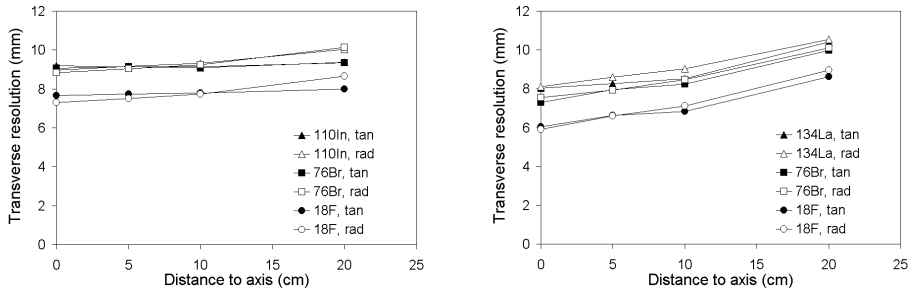

Figure 5.1: *Transaxial resolution vs. distance to centre of FOV for the 4096 (left) and HR+ in 2D mode (right), FWHM, in polythene.*

Table 5.1: *5 cm off-centre transaxial resolution (mm), FWHM (FWTM), 4 mm Hann filter.*

Nuclide	4096 (2D)	HR+ (2D)	HR+ (3D)
^{18}F	7.6 (14.1)	6.6 (12.2)	6.6 (12.1)
^{76}Br	9.1 (18.2)	7.9 (17.0)	8.0 (17.2)
^{134}La	-	8.4 (16.6)	8.4 (16.5)
^{110m}In	9.2 (17.3)		
^{52}Fe/^{52m}Mn	8.7 (19.0)[1]		

[1] from the measurement in paragraph 5.2.3 reconstructed applying a 4-mm Hann filter.

5.2.2 Transaxial resolution vs. density [I,II,IV]

Results of resolution measurements in materials of various densities are shown in figure 5.2. Apparently material density has little effect on spatial resolution.

FWTM values increase slightly with decreasing density. An attempt to explain this result will be made in the next paragraph.

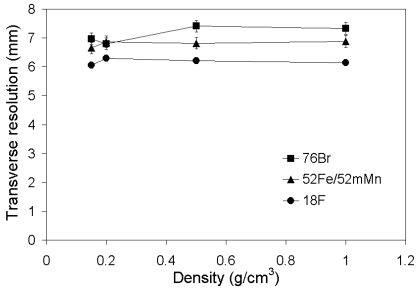

Figure 5.2: *4096+ WB transaxial resolution vs. tissue density for* ^{18}F, ^{76}Br *and* $^{52}Fe/^{52m}Mn$.

5.2.3 Effect of positron range

Levin and Hoffman [81] calculated point spread functions for different nuclides by convoluting one-dimensional functions describing photon noncollinearity, detector size, positron end point distribution, and contributions of light multiplexing in block detectors and undersampling. In a measurement of a thin steel needle line source in air, photon-noncollinearity, detector size, light multiplexing and undersampling in the centre of the FOV all contribute to the measured point spread function $L(x)$. For the 4096 system $L(x)$ can be approximated by a gaussian with an FWHM of 5.83, as measured with a thin steel needle line source in air and reconstructed with a 1-mm ramp filter. The $PSF(x)$ of the image of a near tissue-equivalent line source could then be described as the convolution of this "optimal" point spread function $L(x)$ with the positron range distribution $P(x)$:

$$PSF(x) = L(x) \otimes P(x) \tag{5.1}$$

For calculation of $P(x)$, the positron energy distributions in figure 2.5 were translated to positron end point distributions in unit density material using an energy-range relation for beta particles [33] [1]:

$$E = 5.9(r + 0.007)^{0.565} + 0.00413r^{1.33} - 0.367. \tag{5.2}$$

The resulting distributions are one-dimensional and were transformed to a three-dimensional distribution by division with the square of the distance. The result is

[1] Cole's energy-range relationship for electrons; the error made by applying it to positrons was neglected for the purpose of the calculations presented here.

the positron end point distribution of a point source which was integrated along a line to obtain a line source distribution. Projection of this two dimensional line source positron end point distribution to one dimension then gives $P(x)$. Since the range for beta particles, expressed in cm^2/g, is approximately material-independent [76], the positron end point distribution in other than unit density materials can be found by multiplying the range for a certain energy with the reciprocal of the density. Figure 5.3 shows the positron end point distributions and the point spread functions calculated as described in equation 5.1. The FWHM and FWTM of these PSFs are given in Table 5.2, and compared to measured values.

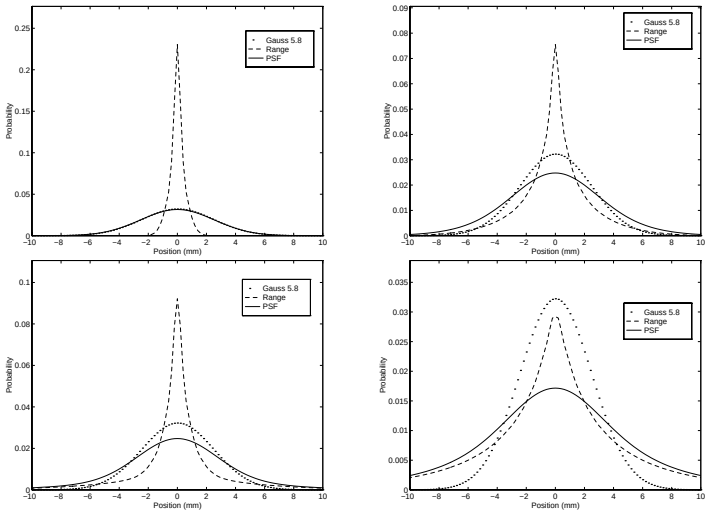

Figure 5.3: *Line source positron end point distributions and point spread functions for ^{18}F (top) and ^{76}Br (bottom) in 1.0 g/cm^3 (left) and 0.2 g/cm^3 (right).*

The calculated FWHM values for ^{18}F and ^{76}Br in 1 g/cm^3 are close to the measured values. The calculation overestimates resolution for ^{76}Br and ^{18}F in 0.2 g/cm^3. A 1-mm outer diameter of the line source was included in the calculation model by assuming that all positrons with a range of 0.5 mm or less are stopped inside the line source and that all other positrons lose energy corresponding to a range of 0.5 mm. After this modification FWHM (FWTM) for ^{18}F and ^{76}Br were 6.0 (10.9) and 7.1 (15.8) mm, respectively. The near density-independence of resolution found in paragraph 5.2.3 can thus be explained by the line source thickness and density.

Table 5.2: *Calculated and measured 4096 central transaxial spatial resolution (mm). FWHM ± SD (FWTM ± SD). Standard deviations are of the mean of the measured resolution in all slices.*

	^{18}F	^{76}Br
1.0 gcm^{-3}	6.0 (10.9)	7.0 (14.6)
measured	6.2 ± 0.2 (11.7 ± 0.3)	7.3 ± 0.2 (16.6 ± 0.4)
0.2 gcm^{-3}	7.3 (14.4)	9.5 (23.3)
measured	6.3 ± 0.2 (12.0 ± 0.2)	6.8 ± 0.2 (18.0 ± 1.0)

5.2.4 Discussion

The relatively large pixel sizes used in the resolution measurements introduce an overestimation in the FWHM and FWTM values obtained by interpolation. Firstly the relative number of counts in the peak pixel is an underestimation of the actual peak of the PSF, increasing with increasing pixel size. This leads to an underestimation of the half-maximum and thus an overestimation of the FWHM. Secondly interpolation leads to overestimation of the FWHM values because of the gaussian shape of the theoretical point spread function. Since larger pixel sizes were used in the 4096 transverse resolution measurements, the 4096 FWHM values are more affected than the HR+ FWHM values.

The degradation in spatial resolution for ^{76}Br, ^{110m}In and ^{52}Fe was not as large as expected by Pagani *et al.* [104]. In a three-dimensional positron range distribution, the range associated with the maximum or average positron energy plays a very small roll as the density of annihilation sites decreases with the square of the distance to the source even for a uniform energy distribution.

The central axial resolution can be calculated in a similar way as central transaxial resolution in a 3D situation without septa according to the method of Levin and Hoffman [81]. So for the HR+ in 3D mode the central axial resolution can be expected to be nearly similar to the transaxial resolution because of its near square detectors [22]. Axial resolution or slice thickness in 2D mode is probably not affected much by positron range for the 4096 scanner with its thick slices and septa, but it may be affected more for the thin slices and thin septa of the HR+ system.

5.3 Recovery

5.3.1 Size estimation [V,VI]

Accurate partial volume correction requires that object sizes can be estimated accurately from the PET images [61]. Using the hot sphere phantom, the accuracy of determination of the object size by drawing a ROI at 50% of the maximum pixel radioactivity concentration was assessed. Estimated sizes versus true sizes are shown in figure 5.4.

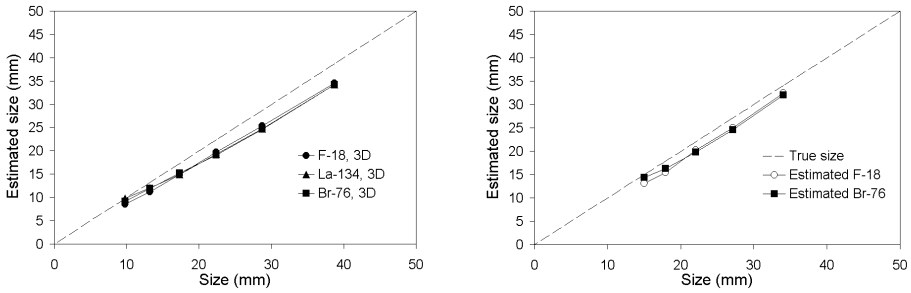

Figure 5.4: *Estimated spheres sizes for three different nuclides (Hann 4.0 filter) with the HR+ (left) and 4096 (right) scanners.*

All estimated object sizes were within 3 mm from the actual object size. There is no significant difference in estimated size between HR+ images reconstructed with a 4 mm Hann filter and a 6 mm Gauss filter, and there is no significant difference between 2D and 3D modes either. For both the 4096 and HR+, the absolute error in estimated size increases with sphere size. Futher measurements are necessary to assess the effect of background radioactivity on this size estimation method for different nuclides.

5.3.2 Hot spot recovery [III,V,VI]

Figures 5.5 and 5.6 show results of recovery measurements for the different PET systems and nuclides. Recovery coefficients for the HR+ were slightly better in 3D mode than in 2D mode. The 4096 recovery coefficients for ^{76}Br and ^{110m}In might be underestimated because figure 5.5 suggests that the largest sphere is not large enough to ensure optimal recovery. The different methods used to calculate recovery coefficients have advantages and disadvantages. The maximum pixel radioactivity concentration is easy to measure, but is sensitive to image statistics (e.g. [51, 74]). The maximum pixel recovery coefficients measured here were rather accurate because of the high radioactivity concentrations in the spheres which resulted in low-noise images. This, however, is usually not the case in

patient studies. The average pixel method gives a lower recovery coefficient but is less sensitive to image statistics. The resolution-sized ROI method is sometimes preferred because it gives nearly nuclide-independent recovery coefficients (figure 5.6 right side). In a study of bias and variance for both maximum pixel and average pixel recovery coefficients, Kohlmyer *et al.* [74] showed that the maximum pixel method may be preferred for objects smaller than 3 cm, whereas the average pixel method may be preferred for larger structures for the filter sizes used in that study, 6 to 12 mm. That study also showed that recovery of small spheres after iterative reconstruction was worse than after FBP. There was no observed difference in recovery coefficients of ^{76}Br images reconstructed with and without correction for gamma radiation coincidences.

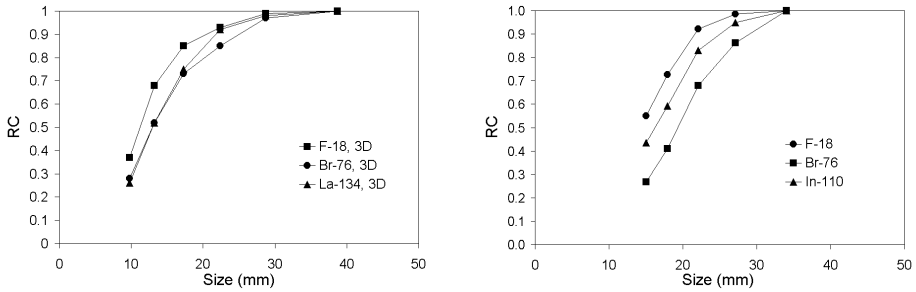

Figure 5.5: *Recovery coefficients vs. sphere size (4 mm Hann filter), measured using a resolution size ROI. Left: HR+. Right: 4096.*

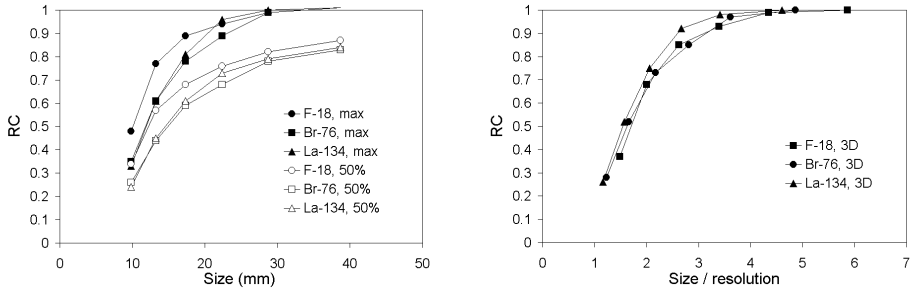

Figure 5.6: *Recovery coefficients vs. sphere size, HR+, measured using the maximum pixel and average pixel methods (left), and measured using a resolution-sized ROI (right). 4 mm Hann filter.*

5.3.3 Cold spot recovery [V]

Figure 5.7 shows measured cold spot recovery of ^{76}Br for the HR+ tomograph. For a linear system hot spot recovery should equal one minus the cold spot recovery [51], which is apparently not true for the HR+ with ^{18}F. If the hot-spot recovery coefficients are divided by 1.08 to account for the remnant correction error in the image, as indicated by the correction accuracy measurements (chapter 4, paper V) and assuming that this remnant correction error is present in the cold spot recovery measurement but not in the hot spot recovery measurement, the system is linear for ^{18}F in 2D mode and also with ^{76}Br provided that a gamma radiation correction is used. In 3D mode, the HR+ recovery is not linear. Gamma radiation correction improves ^{76}Br cold spot recovery considerably, especially in 3D mode.

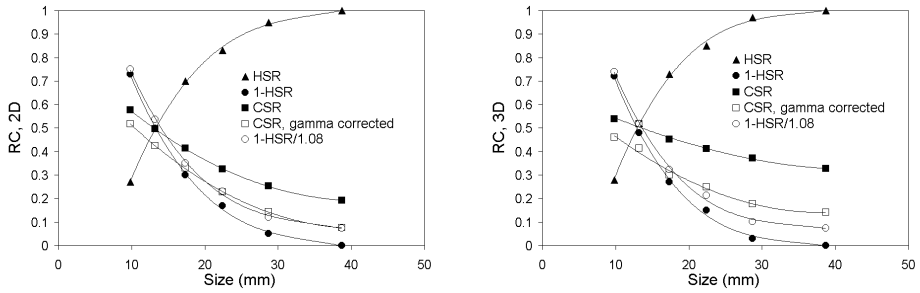

Figure 5.7: *Hot spot (HSR) and cold spot (CSR) recovery coefficients for ^{76}Br calculated using a resolution size ROI. Left: 2D. Right: 3D. Gamma radiation coincidences were subtracted using a linear tail fit.*

5.4 Contrast [V]

For a linear system, the measured radioactivity concentration in a sphere is determined by the following equation:

$$A_{s,m} = RC_{hot} \cdot A_{s,t} + RC_{cold} \cdot A_{b,m} \tag{5.3}$$

where A is the radioactivity concentration, and the indices s, b, t and m denote sphere, background, true, and measured. The measured standard uptake value SUV_m, is then given by:

$$SUV_m = \frac{1}{g} \cdot RC_{hot} \cdot SUV_t + RC_{cold} \tag{5.4}$$

Here g is the overestimation of measured radioactivity caused by gamma coincidences, and SUV_t is the true uptake ratio. This SUV_m can also be seen as

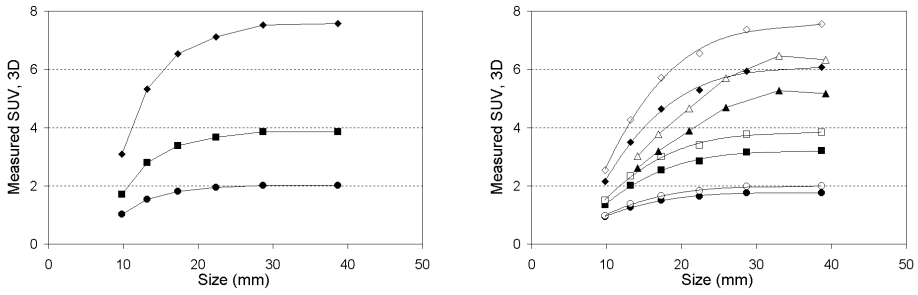

Figure 5.8: *Measured and calculated SUV versus sphere size for actual uptake ratios of 8 (diamonds), 6.5 (triangles; measured), 4 (squares), and 2 (circles). Open symbols are corrected for gamma radiation coincidences. Left:* ^{18}*F. Right:* ^{76}*Br. Gamma radiation coincidences were subtracted using a linear tail fit.*

a measure of contrast. Figure 5.8 shows calculated and measured contrast at different ratios between sphere and background activity for ^{76}Br in 3D mode, both with and without correction for gamma radiation. For the measured data the actual ratio between sphere activity and background activity was approximately 6.5. Gamma radiation correction improves image contrast by more than 15% for the largest spheres, resulting in a similar contrast for ^{76}Br as for ^{18}F. In 2D mode the improvement is smaller but the difference between ^{18}F and ^{76}Br without gamma radiation correction is less than in 3D mode. Clearly, the largest part of the difference in image contrast between ^{76}Br and ^{18}F prior to gamma correction is caused by gamma radiation coincidences.

6. Applications

6.1 ^{110m}In-DTPA-D-Phe^{1}-octreotide [III]

Figure 3 shows standard clinical SPECT and PET images of a patient suffering from a metastasis of a small-intestine carcinoma, 24 h after administration of 175 MBq of ^{111}In-octreotide and 1 h after administration of 140 MBq of ^{110m}In-octreotide.

The PET study consisted of a dynamic series of frames measured during the first two hours after administration of ^{110m}In-octreotide. The standard uptake values calculated from the PET data are given in Figure 6.1. The images clearly show the improved detail in visualisation of the tumour contour and the small structures around the tumour in PET compared to SPECT.

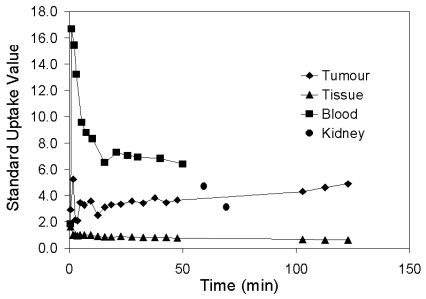

Figure 6.1: *Standard uptake values of ^{110m}In-octreotide in tumour, background tissue, blood and kidney. Error bars are of the same size as markers.*

Central spatial resolution was approximately 9 mm for ^{110m}In-PET and 26 mm for ^{111}In-SPECT, measured on the 4096 PET system and a dual-headed SPECT system (Dynascan, Picker, Cleveland) consisting of two 36x36 cm^2 planar NaI detectors applied with medium energy general purpose (MEGP) collimators. The performance studies in paper IV clearly show the improvement in resolution and recovery that can be obtained with ^{110m}In-PET in comparison to ^{111}In-

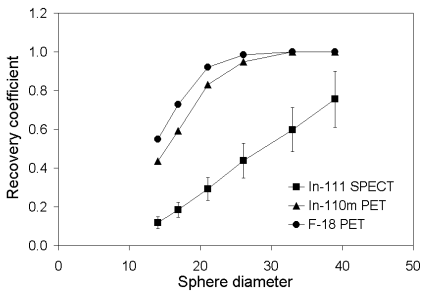

Figure 6.2: *Sphere recovery functions for ^{110}In-PET, ^{111}In-SPECT and, for comparison, ^{18}F-PET. The standard errors in the PET data were less than 5% and the errors in the SPECT data mainly originate from the uncertainty in true radioactivity concentration in the spheres. The true radioactivity concentration in the PET measurement was determined from the ROI in the largest sphere.*

SPECT. An improvement in resolution with almost a factor three would meet the demands on imaging of small tumours or metastases (< 1 cm) as expressed in the literature [82, 117]. The amount of scatter in SPECT measurements causes a major problem in quantification but this can be improved by applying scatter corrections. However, the triple energy window scatter correction used in this study requires good count statistics in the narrow scatter windows, and thus long measurement times.

The initial labelling experiments confirmed that ^{110m}In-DTPA-D-Phe^1-octreotide can be easily prepared using the Octreoscan kit and locally produced ^{110m}In. The availability of the commercial Octreoscan kit solves problems associated with GMP production of the peptide-chelator conjugate and Octreoscan is optimized for labelling with indium isotopes. The low energy required for the ^{110}Cd(p,n)^{110m}In reaction makes it possible to use any commercially available cyclotron for local production of ^{110m}In. The half-life of ^{110m}In is not too short to rule out the possibility to deliver the compound to satellite PET centers that do not have their own cyclotron for radionuclide production.

The clinical imaging study shows that ^{110m}In-octreotide can be employed in studies with positron-emission tomography. The 69-min half-life of ^{110m}In matches the rapid kinetics of octreotide well. The images and uptake curves clearly show the fast blood clearance and kidney uptake of ^{110m}In-octreotide, and a tumour-to-background uptake ratio of eight was reached after two hours. Kinetics were followed for only up to two hours but a measurement time of four hours may be possible without increasing patient dose.

The introduction of the positron-emitting analogue ^{110m}In could help to obtain more precise values of the radioactivity concentration in tumours as well as in critical organs of a given patient and thus aid in the determination of

the absorbed dose in radionuclide therapy with ^{111}In. Similar half-lives of the positron-emitting and the therapeutic isotopes facilitate the calculation of the radioactivity integral, which is needed to obtain a good estimate of the absorbed dose. This is the case for the isotopic pairs ^{90}Y/^{86}Y and ^{131}I/^{124}I, but not for ^{111}In/^{110m}In. However, the half-life of ^{110m}In is long enough to measure the first 3-4 h of the octreotide kinetics in the individual patient. After this the radionuclide distribution is changing relatively slowly, and measurements of ^{111}In with gamma camera techniques can be used to obtain later kinetics. These measurements can then be related to the detailed quantitative PET measurements. Although PET gives a spatial resolution below 1 cm^3, still only macroscopic dose information is obtained. An important part of the dose delivered by ^{111}In is due to the Auger and conversion electrons emitted in its decay. Biopsies and other studies have to be added if a more detailed dosimetry on the cellular level is required. Nevertheless, being able to determine an accurate macroscopic dose is an important first step in the understanding of the dose-effect relation of this type of therapy.

6.2 Quantification of ^{52}Fe [IV]

6.2.1 Manganese correction model

As mentioned previously (chapter 2) ^{52}Fe decays to the also positron-emitting ^{52m}Mn. The distribution of manganese *in vivo* has been studied previously in animal models [24, 115]. It is known that manganese is mainly taken up in liver, heart and lung, and that after a fast blood clearance in the first minutes after administration equilibrium is established between these organs and the blood. Because of the fast physical decay and blood clearance of manganese compared to iron [17, 24], the manganese concentration in blood is determined by an equilibrium between production by iron decay and removal by both manganese decay and uptake in organs. Buck and co-workers [24] have measured organ-to-blood uptake ratios for manganese in pigs. Assuming that these values can also be used in humans it is essential to know the contribution of ^{52m}Mn to the measured radioactivity concentration in blood. When a blood sample is taken, the ^{52}Fe/^{52m}Mn equilibrium is disturbed and the ^{52m}Mn radioactivity starts to increase towards physical equilibrium. This process can be followed with spectroscopic measurements. Practically all gamma radiation from a ^{52}Fe/ ^{52m}Mn sample with energy above a certain energy threshold originates from ^{52m}Mn. The count rate above this energy threshold from a blood sample collected at time t=0 is then given by:

$$fA_{Mn} = fA_{Mn,0}e^{-\lambda_{Mn}t} + f\frac{\lambda_{Mn}}{\lambda_{Mn}-\lambda_{Fe}}A_{Fe,0}(e^{-\lambda_{Fe}t} - e^{-\lambda_{Mn}t}) \qquad (6.1)$$

where f is the detected fraction of the radiation emitted by ^{52m}Mn, and $A_{Mn,0}$ and $A_{Fe,0}$ are the ^{52m}Mn and ^{52}Fe radioactivity at the time of the collection of

the sample. Equation 6.1 was fitted to the measured count rates and the ratio $A_{Mn,0}/A_{Fe,0}$ was calculated.

In theory we could use tissue samples to measure the contribution of ^{52m}Mn in different organs in a similar way. This would require biopsies for each investigation and is therefore not a realistic option. However, an estimation of the manganese contribution can be made using a model based on data on manganese and iron uptake from previous investigations. The ^{52m}Mn concentration in an organ is assumed to be a sum of two contributions: "free manganese", defined as ^{52m}Mn produced by ^{52}Fe decay in the blood, and "bound manganese", defined as ^{52m}Mn produced by intracellular decay of ^{52}Fe in organs. "Free manganese" is quickly cleared from the blood after which a steady organ-to-blood ratio exists in certain organs [24], mainly heart, liver and lungs. The "free manganese" contribution to the activity measured in these organs can then be estimated via this organ-to-blood ratio and the measured ^{52m}Mn/^{52}Fe ratio in blood. "Bound manganese" is assumed to stay inside the cell where it was produced and an equilibrium establishes between iron and "bound manganese". A_{PET}, which is the radioactivity concentration measured by PET in a certain organ at time t, can then be described as:

$$A_t^{PET} = A_{Fe,t}^{PET} + A_{Mn,bound,t}^{PET} + A_{Mn,free,t}^{PET} \tag{6.2}$$

The right side describe the contributions of ^{52}Fe, "bound manganese", and "free manganese", respectively, and each of these can be calculated based on the assumptions above. This results in the following relation between the ^{52}Fe radioactivity concentration in an organ and the organ and blood radioactivity concentrations directly determined from the PET images:

$$A_{Fe,t} = 0.639 A_t^{PET} - \frac{0.639cR}{0.574 + R} A_t^{PET,blood} \tag{6.3}$$

Here, c is the organ-to-blood ratio of "free manganese" for the organ in question, R is the A_{Mn}/A_{Fe} ratio in blood, $A_{Fe,t}$ is the ^{52}Fe-radioactivity concentration in the organ, and A_t^{PET} and $A_t^{PET,blood}$ are the measured radioactivity concentrations in organ and blood, respectively. This equation simplifies in the bone marrow and the spleen where no "free manganese" uptake is expected, making the last term zero.

6.2.2 Patient study

Approximately 10 MBq of a solution of ^{52}Fe-labeled iron-sucrose with ^{52}Fe and ^{52m}Mn in equilibrium was administered to a healthy volunteer (female, age 38, 52 kg). The person was positioned in the 4096+ scanner so that heart, liver and spleen were situated inside the field of view. A dynamic PET study was performed for a period of 8 h after administration. After 1 h a blood sample was taken for determination of the relative amount of ^{52m}Mn activity in the blood. The ^{52m}Mn/^{52}Fe ratio in this blood sample was found to be 0.31 $\pm$ 0.01. After

reconstruction of the PET data applying all standard corrections VOIs were drawn in liver, bone marrow, spleen and heart muscle. Correction for partial volume effect was not applied and data was not corrected for gamma radiation coincidences. All PET data and blood measurements were corrected for ^{52m}Mn radioactivity using the model described above. The organ-to-blood ratios of "free manganese" in liver and heart muscle were assumed to be 4 and 2.5, respectively [24]. The sum of the fractions of injected radioactivity in all relevant organs was calculated before and after correction for ^{52m}Mn (figure 6.3). The organ masses were calculated using the relative organ masses in the ICRP standard adult female phantom (International Commission on Radiological Protection, 1975).

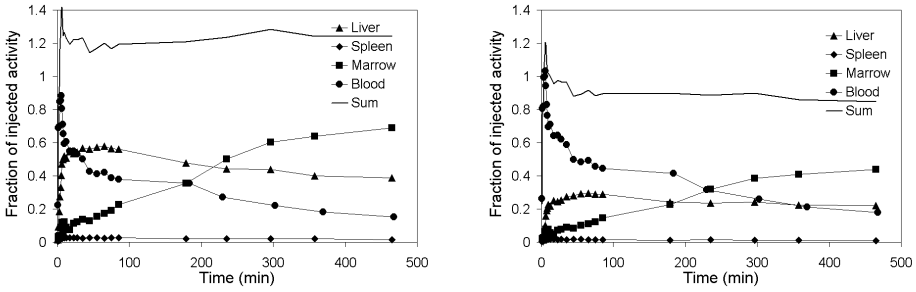

Figure 6.3: *Fraction of injected radioactivity, decay corrected, in liver, spleen, bone marrow and blood, and the sum of these fractions, not corrected (left) and corrected (right) for ^{52m}Mn.*

6.2.3 Evaluation

The applied ^{52m}Mn corrections in organs are not valid before equilibrium is established. This is obvious in figure 6.3, which shows an overestimation of the total ^{52}Fe radioactivity during the first part of the measurement. Another uncertainty in the correction model is the ^{52m}Mn contribution to the blood radioactivity which may vary during the measurement. As mentioned above, determination of individual and time-dependent ^{52m}Mn/^{52}Fe blood ratios is an option, but the gain may be limited without a more reliable organ-to-blood ratio of "free manganese".

The radioactivity uptake in the heart is of special interest because no iron uptake is expected in the heart. The study by Buck and co-workers [24] with free ^{52m}Mn showed a relatively high uptake of manganese in the heart muscle, with an activity concentration of about 2.5 times the blood activity. Using the measured "free manganese" blood radioactivity concentration, the expected radioactivity in the heart muscle was calculated. This expected value was found to be consistent with the PET activity measured in a ROI in the heart muscle, as shown in figure

6.4. The underestimation during the first hour is expected because of the larger concentration of free ^{52m}Mn in the blood directly after administration. This result gives an indication for both the accuracy of the correction for the ^{52m}Mn radioactivity in the blood and the accuracy of our model for correction of "free manganese" uptake in organs.

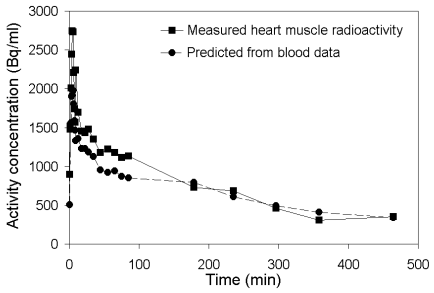

Figure 6.4: *Predicted and measured ^{52m}Mn-radioactivity concentration in the heart muscle.*

After careful corrections quantification is possible in organs with no "free manganese" uptake, such as the bone marrow. The achievable accuracy is slightly worse in blood because of the uncertainty in the ^{52m}Mn contribution, but can be improved with more frequent blood sampling. In organs like the liver, with extra "free manganese" uptake, accurate quantification is more difficult and has to be based on assumptions about the extra ^{52m}Mn contribution and on the measured manganese concentration in blood, which makes quantification more difficult. In this case the best achievable accuracy is determined by the accuracy in the measurement of the manganese concentration in blood and on the assumptions on manganese organ-to-blood ratios used in the model described. These assumptions should be verified in studies of human volunteers. Preferably, manganese kinetics should be measured in each patient prior to the iron study.

6.3 Dosimetry of ^{76}Br-labelled antibodies [II]

This study was done to investigate normal tissue dosimetry of a ^{76}Br-labelled monoclonal antibody with pigs as an experimental model, in order to compare patient dose in radioimmunoimaging with ^{76}Br to patient dose in similar studies with other nuclides.

6.3.1 Animal study

Three SPF Göttingen mini-pigs (Ellegårds Førsøgsgrise, Denmark) were used. The anaesthetised animals were placed in the 4096 scanner and transmission

scans were made over five consecutive regions ranging from the thorax to the kidneys and intestines. After injection of a 46-75 MBq ^{76}Br-38S1 solution a dynamic 1-h scan over the region containing heart, lungs and liver was made. This was followed by cyclic scanning over all regions during a 17.5-h period. Blood samples were collected at various time points to measure blood and plasma radioactivity. Urine samples were collected at 6 h and 15 h after injection. All urine after administration was collected for measurement of the total excreted radioactivity and at the end of the measurements the pigs were sacrificed and dissected for measurement of radioactivity in tissue samples. Images were reconstructed using all standard corrections. Data was not corrected for gamma radiation coincidences. VOIs were drawn in each of the organs of interest, and the blood data measured in the left ventricle of the heart were corrected for partial volume effect by division with a factor 0.8 [86].

Dosimetry

To estimate the radiation dose in humans similar kinetics and distribution in humans as those found in pigs were assumed. Time-activity curves were derived from PET data in blood, lungs, liver, red bone marrow, spleen, kidneys, intestine, and remainder of the body. Exponential extrapolations from the last four non-decay corrected frames were used to estimate the time-activity curve after the last scan. The accumulated activity was calculated by numerical integration of the radioactivity concentration data multiplied with the organ masses in the standard MIRD 70 kg adult phantom [129]. Residence times were calculated as the ratio of the accumulated activity and the injected activity, scaled with the human body weight relative to the weight of the pig. These data were used as input in Mirdose 3 [129], applying a dynamic bladder model with urine excretion rates as measured in the animal study and a bladder voiding interval of 4 h.

6.3.2 Results

Mean residence times and absorbed doses in normal organs are given in table 6.1. The highest average dose is 0.84 mGy/MBq in the lungs. The effective dose equivalent was 0.41 (0.03 maximum deviation) mSv/MBq.

The effective dose estimate in a patient study using 100 MBq of ^{76}Br-38S1 is then 40 mSv, or 0.4 mSv/MBq. This is of the same order as previously reported for radioimmunoimaging studies with ^{111}In [26, 91]. For comparison, a value of 0.029 mSv/MBq has been reported for ^{18}F-FDG [40], leading to an effective dose of about 4 mSv for the amounts of radioactivity usually administered. The amount of radioactivity necessary is determined by tumour to tissue contrast as well as the number of positrons emitted per decay. In this aspect, ^{76}Br has an advantage over ^{124}I since its positron abundance is more than twice as high. For a similar amount of activity and a uniform distribution in the body, the dose per positron for ^{124}I is more than five times the dose per positron for ^{76}Br, although the longer half-live of ^{124}I allows a lower amount of radioactivity if long

Table 6.1: *Mean residence times and absorbed doses in normal organs for ^{76}Br-MAb38S1, mean (maximum deviation), n=3*

	Residence time (h)	Dose (mGy/MBq)
Blood	11 (2)	
Lungs	1.6 (0.4)	0.84 (0.16)
Liver	2.1 (0.9)	0.74 (0.28)
Red bone marrow	0.7 (0.2)	
Spleen	0.037 (0.003)	
Kidneys	0.06 (0.02)	
Small intestine	0.6 (0.2)	
Gall bladder wall		0.38 (0.03)
Upper large intestine wall		0.34 (0.04)
Adrenals		0.34 (0.03)
Pancreas		0.34 (0.04)
Heart wall		0.33 (0.05)
Ovaries		0.32 (0.05)
Uterus		0.32 (0.05)
Total body	23.3 (0.1)	0.27 (0.01)

scan times can be applied. Since the VOI data in organs were not corrected for partial volume effects, the absorbed dose to the bone marrow, a radiosensitive organ, was probably underestimated, also due to the fact that the VOI also included dense vertebral bone. Quantitative accuracy was affected because of gamma radiation coincidences for which no correction was available at the time of this study, although this effect is relatively small for the 4096 tomograph (see Chapter 4, paper V).

6.4 Dosimetry of post-operative ^{131}I-EGF radionuclide therapy of glioma by simultaneous administration of ^{124}I-EGF [I]

6.4.1 Count rate considerations

In addition to the use of PET for dose-planning using diagnostic amounts of radioactivity prior to radionuclide therapy, the use of PET for dose evaluation during radionuclide therapy by adding a small amount of positron-emitting analogue to the administered therapeutic nuclide can be considered.

In a planned study of glioma patients, EGF-dextran labelled with ^{131}I is

administered directly into the surgery cavity with the idea to find and kill spread remains of the tumour [18]. Since the distribution and kinetics of the given ligand are important for determination of the absorbed dose, the possibility to use PET for accurate measurements was considered. A combination of diagnostic amounts of ^{124}I and therapeutic amounts of ^{131}I will be administered.

The large number of single gamma emitted by therapeutic amounts of ^{131}I may disturb the quantitative accuracy of the ^{124}I measurement. To assess this effect the following experiment was performed. A 370 MBq ^{68}Ge/^{68}Ga pin source was combined with a point source containing ^{113m}In ($t_{1/2}$ = 99.5 min) with a starting activity of 5.85 GBq. ^{113m}In was chosen because of the energy of the gamma radiation it emits, 392 keV, is close to the main ^{131}I gamma radiation energy, 364 keV, and because its short half-life allowed the single gamma load to be varied over a large range.

The results showed that the 4096 tomograph saturated at approximately 2.5 GBq of ^{113m}In radioactivity. This is understandable because the singles count rate is the major contributor to the dead time and the 4096 system saturates at about 1.3 GBq [122] of a positron emitter. In the light of the count rate linearity studies in chapter 4 [V] the much increased singles-to-prompts ratio for this application could lead to an overestimation of the dead time by the dead time correction which the results in paper I also indicate.

This situation is highly simplified compared to a patient study and the results can not directly be extrapolated since ^{113m}In was concentrated in the centre of the tomograph. A distributed source in an absorbing material should allow even more radioactivity in the FOV. To understand how the saturation radioactivity of 2.5 GBq is related to the amounts of ^{131}I necessary in therapy the following considerations were made.

Considering beta radiation only, the self-dose S-value of a hollow sphere with inner radius R and thickness d can be calculated as follows:

$$S \approx 0.029[\frac{4}{3}\pi((R+d)^3 - R^3)]^{-1} \tag{6.4}$$

with R and d in cm and the constant 0.029 in [mGy·cm^3/MBq·s]. In paper I a proportionality constant of 0.034 was found by a linear least-squares fit of self-dose S-values versus volumes calculated in Mirdose 3 [129], and an additional contribution of about 15% due to gamma radiation seems reasonable. Based on these S-values the amount of radioactivity that has to be administered to a hollow sphere to obtain a dose of 60 Gy ranges from 51 MBq, assuming a residence time of 96 h for a sphere with an inner diameter of 2 cm and a thickness of 0.5 cm, to 13 GBq, assuming a residence time of 12 h for a sphere with an inner diameter of 5 cm and a thickness of 2 cm. These calculations presume instant uptake of all radioactivity into the area surrounding the cavity so the calculated amounts of radioactivity needed to obtain a tumour dose of 60 Gy are probably underestimated.

A 10:1 radioactivity mixture of ^{131}I/^{124}I emits 106% gamma radiation including annihilation photons and 2.3% positrons per decay. This would result in a

singles rate of about half of the singles rate of a positron-only emitter with the same radioactivity. Considering the saturation of the PET system at 1.3 GBq for positron-only emitters the maximum amount of this ^{131}I/^{124}I mixture would be 2.5 GBq. The maximum possible amount of ^{131}I/^{124}I in 3D mode would be around 300 MBq since 3D systems typically saturate at about one eighth of the activity at which 2D systems saturate. Assuming not too large volumes and a residence time in the order of days a therapeutic amount of ^{131}I should not disturb accurate 2D PET measurements. In addition, the total absorbed dose for this type of therapy will probably not be delivered by radionuclide therapy only but by a combination of radionuclide therapy with external irradiation [18] which decreases the necessary amounts of radioactivity.

Pentlow and co-workers [109] suggested an increase of the GE Advance detection threshold to 400 keV during ^{124}I-PET studies of patients undergoing ^{131}I-radioimmunotherapy to improve image quality. This would certainly lead to a decrease in random coincidences and consequently a better signal to noise ratio in the images. A decrease in sensitivity for true coincidences would also be a consequence but that is hardly a consideration for these types of studies. On the other hand, also singles that are rejected by the energy discriminator contribute to dead time so there would only be a small improvement of the saturation limit (chapter 4).

6.4.2 Dose-kernel based calculation of radiation dose images (ongoing work)

For accurate calculation of absorbed doses for ^{131}I-EGF glioma therapy, non-uniform patient-specific dose calculations are required. Figure 4 shows activity, attenuation and dose images calculated using a computer program developed in the course of this work.

The input required by the program is a series of Scanditronix format images registered to a single attenuation map using existing software (e.g. [6, 7]), as well as various other parameters such as the nuclide used in the PET measurement and the nuclide for which doses should be calculated. The output images can be viewed and analysed using the Scanditronix IDA tool.

The number of decays in each voxel is calculated by numerical integration and the tail of the time-activity curve is calculated using an effective decay constant supplied by the user. Beta absorbed doses are calculated as the product of the number of decays in each voxel and the average beta energy per decay, and then divided by the voxel density. Beta doses are thus assumed to be local. Voxel mass is determined by segmentation of the attenuation image into normal tissue, bone, lungs and air and assignment of the appropriate density to each voxel.

Photon absorbed doses are calculated by convolution of the integrated activity matrix with point dose kernels by Furhang *et al.* [48]. A ^{68}Ga dose kernel, adjusted for positron abundance, is used for all positron-only emitters. To estimate the dose originating from radioactivity directly outside the FOV the data

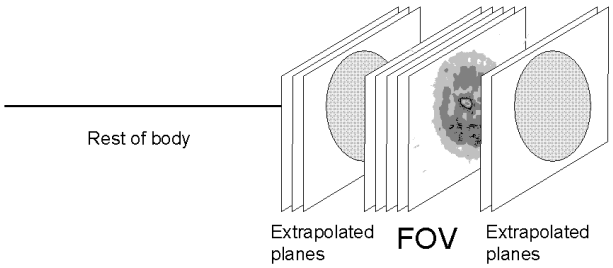

Figure 6.5: *Photon absorbed dose calculation.*

in non-zero density pixels in the first and last slices is uniformly extrapolated to a number of adjacent slices (figure 6.5). The number of extrapolated slices depends on the patient position in the tomograph and is fifteen at maximum. The influence of radioactivity outside the extended image set is estimated by attributing the radioactivity in the rest of the body to a line source and calculating the dose from each 1-cm length interval on this line source to each voxel in the image. To speed up calculations the pixel size is enlarged four times. A density of 1 g/cm^3 in all voxels is assumed in the gamma dose calculations and the dose kernels are not scaled for different attenuation factors. After the convolution the gamma dose images are resampled to the original pixel size and convoluted with a 3x3 pixel mean filter.

The assumption that the rest of the body can be regarded as a line source is probably appropriate for brain studies. In the brain the accuracy of the local dose obtained by this method is then mainly determined by the time covered by the series of PET scans, the spatial resolution, and the accuracy of the effective half-life after the last PET scan. The assumption that all beta doses are deposited locally is not entirely accurate in small voxels for high-energy beta emitters such as ^{90}Y, and dose calculation using the MIRD voxel S-values [19] could be considered. Application of this program for regions where organs with large uptake are just outside the FOV could lead to large errors in gamma-dose. This may be the case for brain studies using ^{124}I due to uptake in the thyroid. Furthermore, density variations lead to errors in gamma dose due to the limitations of the photon dose kernel method. More validation by comparison with other dose calculation programs is necessary.

6.5 ^{134}Ce/^{134}La for radionuclide therapy with Auger-electrons and positrons [VI]

Figure 6.6 shows sphere self-doses for spheres uniformly filled with ^{90}Y, ^{131}I, ^{111}In and ^{134}Ce/^{134}La, calculated using Mirdose 3 [129]. Apparently ^{134}Ce/^{134}La is

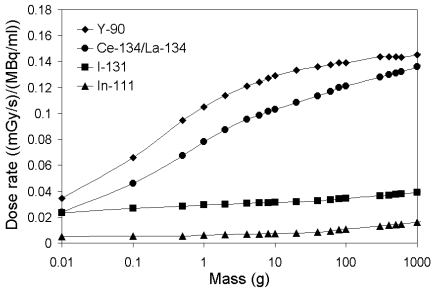

Figure 6.6: *Self-doses to spheres uniformly filled with* ^{90}*Y,* ^{131}*I,* ^{111}*In and* ^{134}*Ce/*^{134}*La.*

Table 6.2: Absorbed dose to the cell nucleus (mGy/Bq.s) for a 14-mm diameter cell with a 10-mm diameter nucleus and different ratios of radioactivity in the cell nucleus to total cell. Based on data in [63]

Nuclide	0%	10%	20%
^{134}Ce/^{134}La	0.163	0.368	0.573
^{134}Ce	0.085	0.232	0.378
^{134}La	0.078	0.136	0.195
^{90}Y	0.091	0.106	0.121
^{111}In	0.165	0.297	0.428

as efficient as ^{131}I for small tumours and superior to ^{131}I for larger tumour sizes. Doses from ^{90}Y are 10% to 30% higher because of the higher beta abundance of ^{90}Y. Table 6.2 gives cellular doses for ^{134}Ce/^{134}La, ^{111}In and ^{90}Y based on MIRD cellular S-value data [63]. With increased translocation to the cell nucleus, the advantage of ^{134}Ce/^{134}La over ^{90}Y and ^{111}In in dose to cell nucleus increases which indicates a higher efficiency in eradication of single cells.

Macroscopic absorbed doses for ^{90}Y, ^{111}In and ^{134}Ce/^{134}La are shown in table 6.3. These absorbed doses were calculated by applying literature data for ^{111}In-octreotide kinetics [8] to each of these nuclides. The macroscopic dose from ^{134}Ce/^{134}La results almost entirely from the positrons and annihilation photons emitted by ^{134}La. The annihilation photons cause a non-specific increase of total-body dose of 26% compared to ^{90}Y but on the other hand they enable accurate dosimetry and improved treatment planning using PET. No PET count rate problems are expected because tumour absorbed doses of several Gy could be

Table 6.3: Macroscopic absorbed doses from ^{111}In, ^{90}Y, ^{134}Ce and ^{134}La; mGy/MBq

	^{111}In	^{90}Y	^{134}Ce/La	^{134}La	^{134}Ce	$\beta+$	La+Ce/Y
Total body	0.09	0.38	0.48	0.47	0.01	0.36	1.26
Liver	0.61	4.54	5.07	4.94	0.13	4.21	1.12
Spleen	0.53	5.53	5.73	5.61	0.12	5.10	1.04
Kidney	0.39	3.60	3.75	3.67	0.08	3.24	1.04
Red marrow	0.07	0.25	0.35	0.34	0.01	0.23	1.40
Tumour (20g)[1]	0.71	11.6	11.1	10.9	0.18	11.0[2]	0.95
Tumour (100g)[1]	0.98	12.1	12.4	12.2	0.21	11.5[2]	1.02
Tumour/Total body ratio	10.9	31.8	25.8				
Tumour/Kidney ratio	2.5	3.4	3.3				

[1] Self-dose only

[2] Using ^{90}Y S-values multiplied by ratio in positron-energy per decay

achieved by administration of several hundred MBq according to table 6.3, and the 4096 saturation limit of 1.3 Gy would correspond to a kidney absorbed dose of nearly 5 Gy.

These results indicate that ^{134}Ce/^{134}La should be as efficient for radionuclide therapy of bulk tumours as ^{90}Y and more efficient than ^{90}Y for treatment of spread cells and micrometastases. In this discussion, the relative biological effectiveness of Auger electrons when emitted close to the DNA was not considered. The models used for the calculations are obviously highly schematic but the results give a good indication of the therapeutic possibilities of ^{134}Ce/^{134}La compared to other nuclides, and justify further investigations.

7. Summary and conclusions

In this work, the PET performance and quantitative applications of a number of positron-emitting nuclides other than the commonly used ^{18}F, ^{11}C or ^{15}O were investigated. A number of conclusions can be made.

Compared to ^{18}F, PET resolution degrades by 1-2 mm FWHM for the high-energy positron emitters ^{76}Br, ^{52m}Mn, ^{110m}In and ^{134}La, and there is a small deterioration in recovery. The effect of positron energy on spatial resolution is less than previously expected in the literature.

The gamma radiation emitted simultaneously with positrons in the decays of ^{76}Br, ^{52m}Mn and ^{110m}In causes a background in PET images leading to a worse quantitative accuracy. For central objects, subtraction of gamma radiation coincidences by a linear fit to the projection tails leads to overall correction accuracy similar for ^{76}Br as for ^{18}F. Delayed coincidence sinograms have approximately the same shape as gamma radiation coincidence sinograms. They can after appropriate scaling and smoothing be used to correct for gamma radiation with similar results as tail fit subtraction. Inclusion of correction for cascade gamma coincidences in 2D convolution backprojection or in 3D model based scatter correction should be considered.

The standard dead time correction of the HR+ tomograph is not adequate for nuclides that emit gamma radiation. A specific dead time correction for cascade gamma radiation emitting nuclides, also considering singles outside the energy window, is necessary.

PET studies of ^{52}Fe yield images showing the sum radioactivity distributions of ^{52}Fe and its decay daughter ^{52m}Mn. A model for correction of measured data for the contribution of ^{52m}Mn was presented, and the results based on one patient study are promising. The assumptions in this correction model should be tested based on actual measured ^{52m}Mn kinetics.

A first clinical imaging study with ^{110m}In-octreotide indicated that PET can be used for imaging of neuroendocrine tumours with better resolution and quantitative accuracy than ^{111}In-octreotide and SPECT. The short half-life of ^{110m}In is no complication because of the fast uptake of octreotide during the first hours after administration.

^{134}Ce/^{134}La may be considered for radionuclide therapy based on Auger electrons and positrons. The calculations presented here indicate tumour self-doses

of the same order as ^{90}Y, and single cell absorbed doses higher than for ^{90}Y. This may be further enhanced if the biological effect of Auger emitters decaying in close vicinity to the DNA is considered. Whole-body dosimetry is less favourable because of the unspecific dose distribution of the annihilation photons from ^{134}La. However, they allow for the use of PET for quantification of the kinetics and thus a more accurate dosimetry which can improve radionuclide therapy.

Patient studies with 100 MBq of ^{76}Br-38S1 would lead to a total body effective dose of circa 40 mSv as extrapolated from animal data. This is of the same order as was reported for clinical radioimmunoimaging studies with ^{111}In.

The amount of radioactivity necessary for post-surgery therapy of glioma with ^{131}I-EGF-dextran does not necessarily lead to singles rates saturating the PET system. Count rate linearity, however, may be affected. More studies on the effects of ^{131}I gamma radiation on count rate linearity of ^{124}I for more realistic radioactivity distributions is necessary.

Several publications have considered the energy of the positrons emitted by ^{76}Br as the main complication for PET measurements, degrading resolution and contrast. The data presented in this work show that the background caused by gamma radiation coincidences and the low noise equivalent count rates at clinically relevant radioactivity concentrations are more important for quantitative accuracy and image contrast. Quantitative accuracy can be improved by applying a correction for cascade gamma radiation coincidences according to the methods described in this work although more refined methods should be considered. On the other hand the highly increased levels of random coincidences, the much lower net trues to gross trues ratio for ^{76}Br compared to ^{18}F, and the low NEC rate are problems that can not be evaded. These lead to increased image noise and consequently a degradation in quantitative accuracy in clinical studies. Noise equivalent count rate can only be improved by increasing patient dose, although never to values near those for ^{18}F or ^{11}C. These conclusions are valid also for ^{52}Fe, although the gamma coincidence fraction and the random fraction should be less. Because of the shorter half-life of ^{110m}In, imaging can be done at higher levels of radioactivity, and consequently at a higher NEC rate, than for ^{76}Br.

Correction of the bias caused by cascade gamma radiation coincidences enables quantitative imaging of ^{76}Br, ^{110m}In, ^{52}Fe and ^{134}La, although with lower signal to noise ratios and with slightly degraded resolution. The applications of these nuclides expand the possibilities of PET and make them interesting complements to the standard PET nuclides.

Bibliography

[1] Adam, L. E., Karp, J. S., and Freifelder, R. Energy-based scatter correction for 3-D PET scanners using NaI(Tl) detectors. *IEEE Trans. Med. Imaging 19* (2000), 513–521.

[2] Adam, L. E., Karp, J. S., and Smith, R. J. Comparison between different performance measurements for PET cameras. In *Future Directions in Nuclear Medicine Physics and Engineering, Chicago, March 19-21, 1999* (Chicago, 1999), J. Aarsvold et al., Eds., The University of Chicago.

[3] Adam, L. E., Zaers, J., Ostertag, H., Trojan, H., Bellemann, M. E., and Brix, G. Performance evaluation of the whole-body PET scanner ECAT Exact HR+ following the IEC standard. *IEEE Trans. Nucl. Sci. 44* (1997), 1172–1180.

[4] Adams, S., Baum, R. P., Hertel, A., Schumm-Draeger, P. M., Usadel, K. H., and Hör, G. Comparison of metabolic and receptor imaging in recurrent medullary thyroid carcinoma with histopathological findings. *Eur. J. Nucl. Med. 25* (1998), 1277–1283.

[5] Anderson, C. J., Dehdashti, F., Cutler, P. D., Schwarz, S. W., Laforest, R., Bass, L. A., Lewis, J. S., and McCarthy, D. W. ^{64}Cu-TETA-octreotide as a PET imaging agent for patients with neuroendocrine tumors. *J. Nucl. Med. 42* (2001), 213–221.

[6] Andersson, J. L. R. *Functional neuroimaging with PET.* Dissertation, Uppsala University, 1995.

[7] Andersson, J. L. R. How to obtain high-accuracy image registration: application to movement correction of dynamic positron emission tomography data. *Eur. J. Nucl. Med. 25* (1998), 575–586.

[8] Andersson, P., Forssell-Aronsson, E., Gretarsdottir, J., Johanson, V., Wängberg, B., Nilsson, O., Fjälling, M., and Ahlman, H. Biokinetics and dosimetry after repeated injections of ^{111}In-DTPA-D-Phe^{1}-octreotide. In *Sixth International radiopharmaceutical dosimetry symposium.* (1999), A. Schlafke-Stelson and E. E. Watson, Eds.

[9] Anger, H. O. Radioisotope camera. In *Instrumentation in nuclear medicine* (New York, 1967), G. J. Hine, Ed., vol. 1, Academic.

[10] Bailey, D. L., and Meikle, S. R. A convolution-subtraction scatter correction method for 3D PET. *Phys. Med. Biol. 39* (1994), 411–424.

[11] Bailey, D. L., Miller, M. P., Spinks, T. J., Bloomfield, P. M., Livieratos, L., Young, H. E., and Jones, T. Experience with fully 3D PET and implications for future high-resolution 3D tomographs. *Phys. Med. Biol. 43* (1998), 777–786.

[12] Bailey, D. L., Young, H., Bloomfield, P. M., Meikle, S. R., Glass, D., Myers, M. J., Spinks, T. J., Watson, C. C., Luk, P., Peters, A. M., and Jones, T. ECAT ART - a continuously rotating PET camera: performance characteristics, initial clinical studies and installation considerations in a nuclear medicine department. *Eur. J. Nucl. Med. 24* (1997), 6–15.

[13] Bendriem, B., and Townsend, D. W. *The Theory and Practice of 3D PET.* Kluwer Academic, Dordrecht, 1998.

[14] Bergström, M., Eriksson, L., Bohm, C., Blomqvist, G., and Litton, J. Corrections for scattered radiation in a ring detector positron camera by integral transformation of the projections. *J. Comput. Assist. Tomogr. 7* (1983), 42–50.

[15] Bergström, M., Lu, L., Fasth, K. J., Wu, F., Bergström-Pettermann, E., Tolmachev, V., Hedberg, E., Cheng, A., and Långström, B. In vitro and animal validation of bromine-76-bromodeoxyuridine as a proliferation marker. *J. Nucl. Med. 39* (1998), 1273–1279.

[16] Beshara, S., Lundqvist, H., Sundin, J., Lubberink, M., Tolmachev, V., Valind, S., Antoni, G., Långström, B., and Danielson, B. G. Kinetic analysis of ^{52}Fe-labelled iron (III) hydroxide-sucrose complex following bolus administration using positron emission tomography. *Br. J. Haematol. 104* (1999), 288–295.

[17] Beshara, S., Lundqvist, H., Sundin, J., Lubberink, M., Tolmachev, V., Valind, S., Antoni, G., Långström, B., and Danielson, B. G. Kinetic analysis and red cell utilization of ^{52}Fe/^{59}Fe-labeled iron (III) hydroxide-sucrose complex following intraveneous administration using positron emission tomography. *Br. J. Haematol. 104* (1999), 296–302.

[18] Blomqvist, E., and Carlsson, J. Strategy for planned radiotherapy of malignant gliomas: postoperative treatment with combinations of high dose proton irradiation and tumor seeking radionuclides. *Int. J. Radiation Oncology 22* (1992), 259–263.

[19] Bolch, W. E., Bouchet, L. G., Robertson, J. S., Wessels, B. W., Siegel, J. A., Howell, R. W., Erdi, A. K., Aydogan, B., Costes, S., Watson, E. E., Charkes, N. D., Fisher, D. R., Hays, M. T., and Thomas, S. R. MIRD pamphlet no. 17: the dosimetry of nonuniform activity distributions – radionuclide S values at the voxel level. medical internal radiation dose committee. *J. Nucl. Med. 40* (1999), 11S–36S.

[20] Boni, R., Blauenstein, P., Dummer, R., Von Schulthess, G. K., Schubiger, P. A., and Steinert, H. C. Non-invasive assessment of tumour cell proliferation with positron emission tomography and [^{76}Br]bromodeoxyuridine. *Melanoma Res. 9* (1999), 569–573.

[21] Borgies, P., Ferrant, A., Leenders, N., Michaux, J. L., Bol, A., Michel, C., Cogneau, M., and Sokal, G. Diagnosis of heterotopic bone marrow in the metastadium using ^{52}Fe and positron emission tomography. *Eur. J. Nucl. Med. 15* (1990), 761–763.

[22] Brix, G., Zaers, J., Adam, L. E., Bellemann, M. E., Ostertag, H., Trojan, H., Haberkorn, U., Doll, J., Oberdorfer, F., and Lorenz, W. J. Performance evaluation of a whole-body PET scanner using the NEMA protocol. *J. Nucl. Med. 38* (1997), 1614–1623.

[23] Buchert, R., Bohuslavizki, K. H., Fricke, H., Mester, J., and Clausen, M. Performance evaluation of PET scanners: testing of geometric arc correction by off-centre uniformity measurement. *Eur. J. Nucl. Med. 27* (2000), 83–90.

[24] Buck, A., Nguyen, N., Burger, C., Ziegler, S., Frey, L., Weigand, G., Erhardt, W., Senekowitsch-Schmidtke, R., Pellikka, R., Bläuenstein, P., Locher, J. T., and Schwaiger, M. Quantitative evaluation of manganese-52m as a myocardial perfusion tracer in pigs using positron emission tomography. *Eur. J. Nucl. Med. 23* (1996), 1619–1627.

[25] Budinger, T., and Wehrli, F., Eds. *Mathematics and physics of emerging biomedical imaging.* National Academy Press, Washington, 1996.

[26] Buijs, W. C., Massuger, L. F., Claessens, R. A., Kenemans, P., and Corstens, F. H. Dosimetric evaluation of immunoscintigraphy using In-111-labeled monoclonal antibody fragments in patients with ovarian cancer. *J. Nucl. Med. 33* (1992), 1113–1120.

[27] Calonder, C., Würtenberger, P. I., Maguire, R. P., Pellikka, R., and Leenders, K. L. Kinetic modelling of ^{52}Fe/^{52m}Mn-citrate at the blood-brain barrier by positron emission tomography. *J. Neurochem. 73* (1999), 2047–2055.

[28] Casey, M. E., Eriksson, L., Schmand, M., Andreaco, M. S., Paulus, M., Dahlbom, M., and Nutt, R. Investigation of LSO crystals for high spatial resolution positron emission tomography. *IEEE Trans. Nucl. Sci. 44* (1997), 1109–1113.

[29] Casey, M. E., Gadagkar, H., and Newport, D. A component based method for normalization in volume PET.

[30] Chiti, A., Fanti, S., Savelli, G., Romeo, A., Bartolomeo, B., Rodari, M., Graafeiland, B. J. V., Monetti, N., and Bombardieri, E. Comparison of somatostatin receptor imaging, computed tomography and ultrasound in the clinical management of neuroendocrine gastro-entero-pancreatic tumours. *Eur. J. Nucl. Med. 25* (1998), 1396–1403.

[31] Christy, M., and Eckerman, K. Specific absorbed fractions of energy at various ages from internal photon sources. Tech. Rep. ORNL/TM-8381 V1-V7, Oak Ridge National Laboratory, Oak Ridge, Tennessee, 1987.

[32] Chu, S. Y. F., Ekström, L. P., and Firestone, R. B. The Lund/LBNL nuclear data search, version 2.0. *http://nucleardata.nuclear.lu.se/nucleardata/toi/* (1999).

[33] Cole, A. Absorption of 20 eV to 50000 eV electron beams in air and plastic. *Radiation Research 38* (1969), 7–33.

[34] Daghighian, F., Pentlow, K. S., Larson, S. M., Graham, M. C., DiResta, G. R., Yeh, S. D. J., Macapinlac, H., Finn, R. D., Arbit, E., and Cheung, N. K. V. Development of a method to measure kinetics of radiolabelled monoclonal antibody in human tumour with applications to microdosimetry: positron emission tomography studies of iodine-124 labelled 3F8 monoclonal antibody in glioma. *Eur. J. Nucl. Med. 20* (1993), 402–409.

[35] Dahlbom, M., MacDonald, L. R., Eriksson, L., Paulus, M., Andreaco, M., Casey, M. E., and Moyers, C. Performance of a YSO/LSO phoswich detector for use in a PET/SPECT system. *IEEE Trans. Nucl. Sci. 44* (1997), 1114–1119.

[36] Daube-Witherspoon, M. E., Carson, R. E., and Green, M. V. Post-injection transmission attenuation measurements for PET. *IEEE Trans. Nucl. Sci. 35* (1988), 757–761.

[37] De Jong, M., Bakker, W. H., Krenning, E. P., Breeman, W. A., der Pluijm, M. E. V., Bernard, B. F., Visser, T. J., Jermann, E., Behe, M., Powell, P., and Mcke, H. Yttrium-90 and indium-111 labelling, receptor binding and biodistribution of [DOTA0, D-Phe1, Tyr3] octreotide, a promising somatostatin analogue for radionuclide therapy. *Eur. J. Nucl. Med. 24* (1997), 368–371.

[38] Defrise, M., Kinahan, P. E., Townsend, D. W., Michel, C., Sibomana, M., and Newport, D. F. Exact and approximate rebinning algorithms for 3-D PET data. *IEEE Trans. Med. Imaging 16* (1997), 145–157.

[39] DeGrado, T. R., Turkington, T. G., Williams, J. J., Stearns, C. W., Hoffman, J. M., and Coleman, R. E. Performance characteristics of a whole-body PET scanner. *J. Nucl. Med. 35* (1994), 1398–1406.

[40] Deloar, H. M., Fujiwara, T., Shidahara, M., Nakamura, T., Yamadera, A., and Itoh, M. Internal absorbed dose estimation by a TLD method for ^{18}F-FDG and comparison with the dose estimates from whole body PET. *Phys. Med. Biol. 44* (1999), 595–606.

[41] Dupont, S., Semah, F., Loc'h, C., Strijckmans, V., Baulac, M., Samson, Y., and Mazière, B. In vivo imaging of muscarinic cholinergic receptors in temporal lobe epilepsy with a new PET tracer: [^{76}Br]4-bromodexetimide. *J. Nucl. Med. 40* (1999), 935–941.

[42] Ferrant, A., Cogneau, M., Leners, N., Jamar, F., Martiat, P., and Michaux, J. L. ^{52}Fe for additional marrow ablation before bone marrow transplantation. *Blood 81* (1993), 3435–3439.

[43] Ficke, D. C., Hood, J. T., and Ter-Pogossian, M. M. A spheroid positron emission tomograph for brain imaging: a feasibility study. *J. Nucl. Med. 37* (1996), 1219–1225.

[44] Fjälling, M., Andersson, P., Forssell-Aronsson, E., Gretarsdottir, J., Johansson, V., Tisell, L. E., Wängberg, B., Nilsson, O., Berg, G., Michanek, A., Lindstedt, G., and Ahlman, H. Systemic radionuclide therapy using indium-111-DTPA-D-Phe1-octreotide in midgut carcinoid syndrome. *Eur. J. Nucl. Med. 37* (1996), 1519–1521.

[45] Flower, M. A., Al-Saadi, A., Harmer, C. L., McCready, V. R., and Ott, R. J. Dose-response study on thyrotoxic patients undergoing positron emission tomography and radioiodine therapy. *Eur. J. Nucl. Med. 21* (1994), 531–536.

[46] Furhang, E. E., Chui, C. S., Kolbert, K. S., Larson, S. M., and Sgouros, G. Implementation of a Monte Carlo dosimetry method for patient-specific internal emitter therapy. *Med. Phys. 24* (1997), 1163–1172.

[47] Furhang, E. E., Chui, C. S., and Sgouros, G. A Monte-Carlo approach to patient-specific dosimetry. *Med. Phys. 23* (1996), 1523–1529.

[48] Furhang, E. E., Sgouros, G., and Chui, C. S. Radionuclide photons dose kernels for internal emitter dosimetry. *Med. Phys. 23* (1996), 759–746.

[49] Gardelle, O., Roelcke, U., Vontobel, P., Crompton, N. E. A., Guenther, I., Bläuenstein, P., Schubiger, A. P., Blattmann, H., Ryser, J. E., Leenders, K. L., and Kaser-Hotz, B. [^{76}Br]bromodeoxyuridine PET in tumor-bearing animals. *Nucl. Med. Biol. 28* (2001), 51–57.

[50] Germano, G., and Hoffman, E. J. Investigation of count rate and deadtime characteristics of a high resolution PET system. *J. Comput. Assist. Tomogr. 12* (1988), 836–846.

[51] Geworski, L., Knoop, B. O., Knapp, W. H., and Munz, D. L. Feasibility of recovery correction in positron emission tomography (PET). *Eur. J. Nucl. Med. 27* (2000), 1189.

[52] Giap, H. B., Macey, D. J., and Podoloff, D. A. Development of a SPECT-based three-dimensional treatment planning system for radioimmunotherapy. *J. Nucl. Med. 36* (1995), 1885–1894.

[53] Graham, M. C., Pentlow, K. S., Mawlawi, O., Finn, R. D., Daghighian, F., and Larson, S. M. An investigation of the physical characteristics of ^{66}Ga as an isotope for PET imaging and quantitation. *Med. Phys. 24* (1997), 317–326.

[54] Grootoonk, S., Spinks, T. J., Sashin, D., Spyrou, N. M., and Jones, T. Correction for scatter in 3D brain PET using a dual energy window method. *Phys. Med. Biol. 41* (1996), 2757–2774.

[55] Gudjonsson, O., Bergström, M., Kristjansson, S., Wu, F., Nyberg, G., Fasth, K. J., and Långström, B. Analysis of ^{76}Br-BRdU in DNA of brain tumors after a PET study does not support its use as a proliferation marker. *Nucl. Med. Biol. 28* (2001), 59–65.

[56] Guzzardi, R., Bellina, C., Knoop, B., Jordan, K., Ostertag, H., Reist, H., Spinks, T., and Vacher, J. Methodologies for performance evaluation of positron emission tomographs. *Nucl. Med. Biol. 35* (1991), 141–157.

[57] Herzog, H., Rösch, F., Stocklin, G., Lueders, C., Qaim, S. M., and Feinendegen., L. E. Measurement of pharmacokinetics of yttrium-86 labelled radiopharmaceuticals with PET and radiation dose calculations of analogous yttrium-90 radioherapeutics. *J. Nucl. Med. 34* (1993), 2222–2226.

[58] Herzog, H., Rota Kops, E., Schmid, A., and Feinendegen, L. E. Effects of varying physical parameters of a PET system on the accuracy of radioactivity quantitation *in vivo*. *Medical Progress through Technology 17* (1991), 193–198.

[59] Herzog, H., Zilken, H., Niederbremer, A., Friedrich, W., and Müller-Gärtner, H. W. Calculation of residence times and radiation doses using the standard PC software Excel. *Eur. J. Nucl. Med. 24* (1997), 1514–1521.

[60] Herzog, H. R., Hohn, A., Qaim, S. M., Tellmann, L., and Coenen, H. H. Phantom-study to test positron-emitting iodine-120. *J. Nucl. Med. 40* (1999), 124P.

[61] Hoffman, E. J., Huang, S. C., and Phelps, M. E. Quantitation in positron emission computed tomography: 1. Effect of object size. *J. Comput. Assist. Tomogr. 3* (1979), 299–308.

[62] Hornick, C. A., Anthony, C. T., Hughey, S., Gebhardt, B. M., Espedan, G. D., and Woltering, E. A. Progressive nuclear translocation of somatostatin analogs. *J. Nucl. Med. 41* (2000), 1256–1263.

[63] Howell, R. W., Rao, D. V., Bouchet, L. G., Bolch, W. E., and Goddu, S. M. *MIRD cellular S values*. Society of Nuclear Medicine, New York, 1999.

[64] Internation Electrotechnical Commission, IEC 61675-1 (1998-02). Radionuclide imaging devices - characteristics and test conditions - part 1: Positron emission tomographs, 1998.

[65] Jarritt, P. H., and Acton, P. D. PET imaging using gamma camera systems: a review. *Nucl. Med. Comm. 17* (1996), 758–766.

[66] Jones, W. F., Digby, W. M., Luk, W. K., Casey, M. E., and Byars, L. G. Optimizing rod window width in positron emission tomography. *IEEE Trans. Med. Imaging 14* (1995), 266–270.

[67] Karp, J. S., Adam, L. E., Freifelder, R., Muehllehner, G., Liu, F., and Surti, S. A high-resolution GSO-based brain PET camera. In *Conference record, IEEE nuclear science symposium* (1999), vol. 2, pp. 1077–1081.

[68] Karp, J. S., Daube-Witherspoon, M. E., Hoffman, E. J., Lewellen, T. K., Links, J. M., Wong, W. H., Hichwa, R. D., Casey, M. E., Colsher, J. G., Hitchens, R. E., Muehllehner, G., and Stoub, E. Performance standards in positron emission tomography. *J. Nucl. Med. 12* (1991), 2342–2350.

[69] Karp, J. S., Muehllehner, G., Mankoff, D. A., Ordonez, C. E., Ollinger, J. M., Daube-Witherspoon, M. E., Haigh, A. T., and Beerbohm, D. J. Continous-slice PENN-PET: a positron tomograph with volume imaging capability. *J. Nucl. Med.* (1990), 617–627.

[70] Kinahan, P. E., Rogers, J. G., Harrop, R., and Johnson, R. R. Three-dimensional image reconstruction in object space. *IEEE Trans. Nucl. Sci. 35* (1989), 749–752.

[71] Kinsey, R. R. *The NuDat Program for Nuclear Data on the Web, version 2.5, http://www.nndc.bnl.gov/nndc/nudat/.* National Nuclear Data Center, Brookhaven National Laboratory, 1996.

[72] Knoop, B. O., Jordan, K., and Spinks, T. Evaluation of PET count rate performance. *Eur. J. Nucl. Med. 15* (1989), 707–711.

[73] Kohlmyer, S. G., Miyaoka, R. S., Shoner, S. C., Lewellen, T. K., and Eary, J. F. Quantitative accuracy of PET imaging with yttrium-86. *J. Nucl. Med. 40* (1999), 280P.

[74] Kohlmyer, S. G., Vesselle, H., Miyaoka, R. S., Kaplan, M. S., and Lewellen, T. K. Comparison of recovery coefficients for PET based on maximum and average ROI pixel values. *Eur. J. Nucl. Med. 27* (2000), 977.

[75] Kolbert, K. S., Sgouros, G., Scott, A. M., Bronstein, J. E., Malane, R. A., Zhang, J., Kalaigian, H., McNamara, S., Schwartz, L., and Larson, S. M. Implementation and evaluation of patient-specific three-dimensional internal dosimetry. *J. Nucl. Med. 38* (1997), 301–308.

[76] Krane, K. S. *Introductory nuclear physics.* Wiley, New York, 1988.

[77] Krenning, E. P., Kwekkeboom, D. J., Bakker, W. H., Breeman, W. A., Kooij, P. P., Oei, H. Y., van Hagen, M., Postema, P. T., de Jong, M., and Reubi, J. C. Somatostatin receptor scintigraphy with [111In-DTPA-D-Phe1]- and [123I-Tyr3]-octreotide: the Rotterdam experience with more than 1000 patients. *Eur. J. Nucl. Med. 20* (1993), 716–731.

[78] Laitinen, J. O., Kairemo, K. J. A., Jekunen, A. P., Korppi-Tommola, T., and Tenhunen, M. The effect of three dimensional activity distribution on the dose planning of radioimmunotherapy for patients with advanced intraperitoneal pseudomyxoma. *Cancer 80* (1997), 2545–2552.

[79] Larson, S. M., Pentlow, K. S., Volkow, N. D., Wolf, A. P., Finn, R. D., Lambrecht, R. M., Graham, M. C., DiResta, G., Bendriem, B., Daghighian, F., Yeh, S. D. J., Wang, G. J., and Cheung, N. K. V. PET scanning of iodine-124-3F9 as an approach to tumor dosimetry during treatment planning for radioimmunotherapy in a child with neuroblastoma. *J. Nucl. Med. 33* (1992), 2020–2023.

[80] Lebtahi, R., Cadiot, G., Sarda, L., Daou, D., Faraggi, M., Petegnief, Y., Mignon, M., and le Guludec, D. Clinical impact of somatostatin receptor scintigraphy in the management of patients with neuroendocrine gastroenteropancreatic tumors. *J. Nucl. Med. 38* (1997), 853–858.

[81] Levin, C. S., and Hoffman, E. J. Calculation of positron range and its effect on the fundamental limit of positron emission tomography system spatial resolution. *Phys. Med. Biol. 44* (1999), 781–799.

[82] Links, J. M. Advances in nuclear medicine instrumentation: considerations in the design and selection of an imaging system. *Eur. J. Nucl. Med. 25* (1998), 1453–1466.

[83] Litton, J., Bergström, M., Eriksson, L., Bohm, C., Blomqvist, G., and Kesselberg, M. Performance study of the PC-384 positron camera system for emission tomography of the brain. *J. Comput. Assist. Tomogr. 8* (1984), 74–87.

[84] Liu, A., Williams, L. E., Lopatin, G., Yamauchi, D. M., Wong, J. Y. C., and Raubitschek, A. A. A radionuclide therapy treatment planning and dose estimation system. *J. Nucl. Med. 40* (1999), 1151–1153.

[85] Loevinger, R., Budinger, T., and Watson, E. *MIRD primer for absorbed dose calculations.* Society of Nuclear Medicine, New York, 1988.

[86] Lövqvist, A. *On the use of ^{76}Br for radioimmuno PET.* Dissertation, Uppsala University, Uppsala, Sweden, 1996.

[87] Lövqvist, A., Sundin, A., Ahlström, H., Carlsson, J., and Lundqvist, H. ^{76}Br-labeled monoclonal anti-CEA antibodies for radioimmuno positron emission tomography. *Nucl. Med. Biol. 22* (1995), 125–131.

[88] Lövqvist, A., Sundin, A., Roberto, A., Ahlström, H., Carlsson, J., and Lundqvist, H. Comparative PET imaging of experimental tumors with bromine-76-labeled antibodies, fluorine-18-fluorodeoxyglucose and carbon-11-methionine. *J. Nucl. Med. 38* (1997), 1029–1035.

[89] Lundqvist, H., Lubberink, M., Tolmachev, V., Lövqvist, A., Sundin, A., Beshara, S., Bruskin, A., Carlsson, J., and Westlin, J. E. Positron emission tomography and radioimmunotargeting - general aspects. *Acta Oncol. 38* (1999), 335–341.

[90] Lundqvist, H., Tolmachev, V., Bruskin, A., Einarsson, L., and Malmborg, P. Rapid separation of ^{110}In from enriched Cd targets by thermal diffusion. *Appl. Rad. Isot. 46* (1995), 859–864.

[91] Mardirossian, G., Brill, A. B., Dwyer, K. M., Kahn, D., and Nelp, W. Radiation absorbed dose from indium-111-CYT-356. *J. Nucl. Med. 37* (1996), 1583–1588.

[92] Mazière, B., Loc'h, C., Baron, J. C., Sgouropoulos, P., Duquesnoy, N., D'Antona, R., and Cambon, H. In vivo quantitative imaging of dopamine receptors in human brain using positron emission tomography and [^{76}Br]-bromospiperone. *Eur. J. Pharmacol. 114* (1985), 267–272.

[93] Mazière, B., Loc'h, C., Stulzaft, O., Hantraye, P., Ottaviani, M., Comar, D., and Mazière, M. [^{76}Br]-bromolisuride: a new tool for quantitative in vivo imaging of D-2 dopamine receptors. *Eur. J. Pharmacol. 127* (1986), 239–247.

[94] McCarthy, K. E., Woltering, E. A., and Anthony, L. B. In situ radiotherapy with ^{111}In-pentreotide: state of the art and perspectives. *Q. J. Nucl. Med. 44* (2000), 88–95.

[95] McCarthy, K. E., Woltering, E. A., Espenan, G. D., Cronin, M., Maloney, T. J., and Anthony, L. B. In situ radiotherapy with ^{111}In-pentreotide: intitial observations and future directions. *Cancer J. Sci. Am. 4* (1998), 94–102.

[96] McDevitt, M. R., Sgouros, G., Finn, R. D., Humm, J. L., Jurcic, J. G., Larson, S. M., and Scheinberg, D. A. Radioimmunotherapy with alpha-emitting nuclides. *Eur. J. Nucl. Med. 25* (1998), 1341–1351.

[97] Meyers, M. O., Anthony, L. B., McCarthy, K. E., Drouant, G., Maloney, T. J., Espanan, G. D., and Woltering, E. A. High dose ^{111}In pentreotide radiotherapy for metastatic atypical carcinoid tumor. *South. Med. 93* (2000), 809–811.

[98] Muehllehner, G. Positron camera with extended counting rate capability. *J. Nucl. Med. 16* (1975), 653–657.

[99] Muehllehner, G., and Karp, J. S. A positron camera using position-sensitive detectors: PENN-PET. *J. Nucl. Med. 27* (1986), 90–98.

[100] National Electrical Manufacturers Association, NEMA standards publication NU 2-1994. Performance measurements of positron emission tomographs, 1994.

[101] O'Byrne, K. J., and Carney, D. N. Radiolabelled somatostatin analogue scintigraphy in oncology. *Anticancer Drugs 7* (1996), 33–44.

[102] Ollinger, J. M. Model-based scatter correction for fully 3D PET. *Phys. Med. Biol. 41* (1996), 153–176.

[103] Olsen, J. O., Pozderac, R. V., Hinkle, G., Hill, T., O'Dorisio, T. M., Schirmer, W. J., Ellison, E. C., and O'Dorisio, M. S. Somatostatin receptor imaging of neuroendocrine tumors with indium-111 pentetreotide (Octreoscan). *Semin. Nucl. Med. 25* (1995), 251–261.

[104] Pagani, M., Stone-Elander, S., and Larsson, S. A. Alternative positron emission tomography with non-conventional positron emitters: effects of their physical properties on image quality and potential clinical applications. *Eur. J. Nucl. Med. 24* (1997), 1301–1327.

[105] Pentlow, K. S., Finn, R. D., Larson, S. M., Erdi, Y. E., Beattie, B. J., and Humm, J. L. Quantitative imaging of yttrium-86 with PET: the occurence and correction of anomalous apparent activity in high density regions. *Clinical Positron Imaging 3* (2000), 85–90.

[106] Pentlow, K. S., Finn, R. D., Larson, S. M., Erdi, Y. E., and Humm, J. L. Effects of cascade gamma rays in PET imaging and quantitation. *J. Nucl. Med. 40* (1999), 280P.

[107] Pentlow, K. S., Graham, M. C., Lambrecht, R. M., Cheung, N. K. V., and Larson, S. M. Quantitative imaging of I-124 using positron emission tomography with applications to radioimmunotargeting and radioimmunotherapy. *Med. Phys. 18* (1991), 357–366.

[108] Pentlow, K. S., Lambrecht, M. C. G. R. M., Daghighian, F., Bacharach, S. L., Bendriem, B., Finn, R. D., Jordan, K., Kalaigian, H., Karp, J. S., Robeson, W. R., and Larson, S. M. Quantitative imaging of iodine-124 with PET. *J. Nucl. Med. 37* (1996), 1557–1562.

[109] Pentlow, K. S., Mawlawi, O., Daghighian, F., Finn, R. D., Humm, J. L., and Larson, S. M. Imaging of tracer amounts of I-124 in the presence of therapeutic amounts of I-131 with a standard PET scanner. *J. Nucl. Med. 39* (1998), 195P.

[110] Phelps, M. E., Hoffman, E. J., Mullani, N. A., and Ter-Pogossian, M. M. Application of annihilation coincidence detection to transaxial reconstruction tomography. *J. Nucl. Med. 16* (1975), 210–223.

[111] Reilly, R. M., Kiarash, R., Cameron, R. G., Porlier, N., Sandhu, J., Hill, R. P., Vallis, K., Hendler, A., and Gariepy, J. ^{111}In-labeled EGF is selectively radiotoxic to human breast cancer cells overexpressing EGFR. *J. Nucl. Med. 41* (2000), 357–366.

[112] Ribeiro, M. J., Almeida, P., Strul, D., Ferreira, N., Loc'h, C., Brulon, V., Trebossen, R., Mazière, B., and Bendriem, B. Comparison of fluorine-18 and bromine-76 imaging in positron emission tomography. *Eur. J. Nucl. Med. 26* (1999), 758–766.

[113] Ribeiro, M. J., Remy, R., Loc'h, C., Brulon, V., and Trebossen, R. The influence of positron range on the measurement of a physiopatalogical antero-posterior gradient in PET imaging of the putamen. *Eur. J. Nucl. Med. 27* (2000), 1190.

[114] Riggin, S. L., Killroy, K. J., and Smith, R. J. Clinical PET imaging with the C-PET camera. *J. Nucl. Med. Technol. 28* (2000), 23–28.

[115] Robertson, J. S., Price, R. R., Budinger, T. F., Fairbanks, V. F., and Pollycove, M. Radiation absorbed doses from iron-52, iron-55 and iron-59 used to study ferrokinetics. *J. Nucl. Med. 24* (1983), 339–348.

[116] Roelcke, U., Leenders, K. L., Ammon, K. V., Radu, E. W., Vontobel, P., Gunther, I., and Psylla, M. Brain tumor iron uptake measured with positron emission tomography and ^{52}Fe-citrate. *J. Neurooncol. 29* (1996), 157–165.

[117] Ronga, G., Salerno, G., Procaccini, E., Mauro, L., Annovazzi, A., Barone, R., Mellozzi, M., Tamburrano, G., and Signore, A. ^{111}In-octreotide scintigraphy in metastatic medullary thyroid carcinoma before and after octreotide therapy: in vivo evidence of the possible down-regulation of somatostatin receptors. *Q. J. Nucl. Med. 39* (1995), 134–136.

[118] Rösch, F., Blessing, G., Linse, K. H., Herzog, H., and Qaim, S. M. Production of the positron emitting strontium isotope Sr-83 and PET phantom measurements preparatory to the evaluation of Sr-89 pharmacokinetics and dosimetry. *J. Nucl. Med. 37* (1996), 166P.

[119] Rösch, F., Brockmann, J., Lebedev, N. A., and Qaim, S. M. The Auger-electron emitter ^{140}Nd: production and radiochemical separation. *J. Labelled Cpd. Radiopharm. 42* (1999), S927–S929.

[120] Rösch, F., Herzog, H., Plag, C., Neumaier, B., Braun, U., Mueller-Gärtner, H. W., and Stöcklin, G. Radiation doses of yttrium-90 citrate and yttrium-90 EDTMP as determined via analogous yttrium-86 complexes and positron emission tomography. *Eur. J. Nucl. Med. 23* (1996), 958–966.

[121] Rösch, F., Herzog, H., Stolz, B., Brockmann, J., Köhle, M., Mühlensiepen, H., Marbach, P., and Müller-Gärtner, H. W. Uptake kinetics of the somatostatin receptor ligand [^{86}Y]DOTA-D-Phe^{1}-Tyr^{3}-octreotide ([^{86}Y]SMT487) using positron emission tomography in non-human primates and calculation of radiation doses of the ^{90}Y-labelled analogue. *Eur. J. Nucl. Med. 26* (1999), 358–366.

[122] Rota Kops, E., Herzog, H., Schmidt, A., Holte, S., and Feinendegen, L. E. Performance characteristics of an eight-ring whole body PET scanner. *J. Comput. Assist. Tomogr. 14* (1990), 437–445.

[123] Ryser, J. E., Blauenstein, P., Remy, N., Weinreich, R., Hasler, P. H., Novak-Hofer, I., and Shubiger, P. A. [^{76}Br]bromodeoxyuridine, a potential tracer for the measurement of cell proliferation by positron emission tomography, in vivo and in vitro studies. *Nucl. Med. Biol. 26* (1999), 673–679.

[124] Schorm, F. Charakterisierung der instrumentellen Eigenschaften des Positronen-Emissions-Tomographen Siemens/CTI ECAT EXACT HR+. Master's thesis, Fachhochschule Aachen, Abteilung Jülich, 1997.

[125] Sgouros, G., Barest, G., Thekkumthala, J., Chui, C., Mohan, R., Bigler, R. E., and Zanzonico, P. B. Treatment planning for internal radionuclide therapy: three-dimensional dosimetry for nonuniformly distributed radionuclides. *J. Nucl. Med. 31* (1990), 1884–1891.

[126] Shao, L., and Karp, J. S. Modified convolution-subtraction scattering correction technique for 3D PET. In *Conference record, IEEE nuclear science symposium and medical imaging conference* (1995), vol. 3, pp. 1430–1433.

[127] Smith-Jones, P. M., Stolz, B., Bruns, C., Albert, R., Reist, H. W., Fridrich, R., and Maecke, H. R. Gallium-67/gallium-68-[DFO]-octreotide - a potential radiopharmaceutical for PET imaging of somatostatin receptor-positive tumors: synthesis and radiolabeling in vitro and preliminary in vivo studies. *J. Nucl. Med. 35* (1994), 317–325.

[128] Spinks, T. J., Miller, M. P., Bailey, D. L., Bloomfield, P. M., Livieratos, L., and Jones, T. The effect of activity outside the direct field of view in a 3D-only whole-body positron tomograph. *Phys. Med. Biol. 43* (1998), 895–904.

[129] Stabin, M. MIRDOSE: personal computer software for internal dose assessment in nuclear medicine. *J. Nucl. Med. 37* (1996), 538–546.

[130] Stearns, C. Scatter correction method for 3D PET using 2D fitted gaussian functions. *J. Nucl. Med. 36* (1995), 105P.

[131] Strand, S. E., Jönsson, B. A., Ljungberg, M., and Tenvall, J. Radioimmunotherapy dosimetry - a review. *Acta Oncol. 32* (1993), 807–817.

[132] Strother, S. C., Casey, M. E., and Hoffman, E. J. Measuring PET scanner sensitivity: relating countrates to image signal-to-noise ratio using noise equivalent counts. *IEEE Trans. Nucl. Sci. 37* (1990), 783–788.

[133] Tagesson, M., Ljungberg, M., and Strand, S. E. A Monte-Carlo program converting activity distributions to absorbed dose distributions in a radionuclide treatment planning system. *Acta Oncol. 35* (1996), 367–372.

[134] Tiensuu Janson, E., Eriksson, B., Öberg, K., Skogseid, B., Öhrvall, U., Nilsson, S., and Westlin, J. E. Treatment with high dose Octreoscan in patients with neuriendocrine tumors-evaluation of therapeutic and toxic effects. In *Vth Scandinavian meeting on radioimmunotargeting, Umeå, Sweden.* (1998).

[135] Tisell, L. E., Ahlman, H., Wängberg, B., Hansson, G., Molne, J., Nilsson, O., Lindstedt, G., Fjälling, M., and Forssell-Aronsson, E. Somatostatin receptor scintigraphy in medullary thyroid carcinoma. *Br. J. Surg. 84* (1997), 543–547.

[136] Tolmachev, V., Bernardt, P., Forsell-Aronsson, E., and Lundqvist, H. ^{114m}In, a candidate for radionuclide therapy: low-energy cyclotron production and labelling of DTPA-D-Phe-octreotide. *Nucl. Med. Biol. 27* (2000), 183–188.

[137] Tolmachev, V., Lövqvist, A., Einarsson, L., Schultz, J., and Lundqvist, H. Production of ^{76}Br by a low energy cyclotron. *Appl. Rad. Isot. 49* (1998), 1537–1540.

[138] Tolmachev, V., Lundqvist, H., and Einarsson, L. Neutron deficient nuclides for positron emission tomography. Production of iron-52 and iron-52/manganese-52m generator. Tech. rep., Institute for Theoretical and Experimental Physics, Moscow, 1996.

[139] Townsend, D. W., and Defrise, M. Image reconstruction methods in positron tomography. Yellow Report 93-02, CERN, Geneva, Switzerland, 1993.

[140] Townsend, D. W., Wensveen, M., Byars, L. G., Geissbuhler, A., Tochon-Danguy, H. J., Christin, A., Defrise, M., Bailey, D. L., Grootoonk, S., Donath, A., and Nutt, R. A rotating PET scanner using BGO block detectors: design, performance and applications. *J. Nucl. Med. 34* (1993), 1367–1376.

[141] Wängberg, B., Nilsson, O., Johansson, V., Kölby, L., Forssell-Aronsson, E., Andersson, P., Fjälling, M., Tisell, L. E., and Ahlman, H. Somatostatin receptors in the diagnostics and therapy of neuroendocrine tumors. *The Oncologist 2* (1997), 50–58.

[142] Watson, C. C., Newport, D., Casey, M. E., DeKemp, R. A., Beanlands, R. S., and Schmand, M. Evaluation of simulation-based scatter correction for 3D PET cardiac imaging. *IEEE Trans. Nucl. Sci. 44* (1997), 90–97.

[143] Wester, H. J., Brockmann, J., Rösch, F., Wutz, W., Herzog, H., Smith-Jones, P., Stolz, B., Bruns, C., and Stocklin, G. PET pharmacokinetics of ^{18}F-octreotide: a comparison with ^{76}Ga-DFO- and ^{86}Y-DTPA-octreotide. *Nucl. Med. Biol. 24* (1997), 275–286.

[144] Westlin, J. E., Janson, E. T., Arnberg, H., Ahlstrom, H., Oberg, K., and Nilsson, S. Somatostatin receptor scintigraphy of carcinoid tumours using the [^{111}In-DTPA-D-Phe^1]-octreotide. *Acta Oncol. 32* (1998), 783–788.

[145] Wheldon, T. E., and O'Donoghue, J. A. The radiobiology of targeted radiotherapy. *Int. J. Radiat. Biol. 58* (1990), 1–21.

[146] Wheldon, T. E., O'Donoghue, J. A., Barett, A., and Michalowski, A. S. The curability of tumours of differing size by targeted radiotherapy using ^{131}I or ^{90}Y. *Radiother. Oncol. 21* (1991), 91–99.

[147] Wrenn, F. R., Good, M. L., and Handler, P. The use of positron-emitting radioisotopes for the localization of brain tumors. *Science 113* (1951), 525–527.

[148] Wu, F., Yngwe, U., Hedberg, E., Honda, M., Lu, L., Eriksson, B., Watanabe, Y., Bergström, M., and Långström, B. Distribution of (76)Br-labeled antisense oligonucleotides of different lenghts determined ex vivo in rats. *Eur. J. Pharm. Sci. 10* (2000), 179–186.

[149] Xu, M., Cutler, P. D., and Luk, W. K. Adaptive segmented attenuation correction for whole-body PET imaging. *IEEE Trans. Nucl. Sci. 43* (1996), 331–337.

[150] Yamamoto, S., Iida, H., Amano, M., Miura, S., Hirose, Y., and Kanno, I. Count rate capability considerations and results for a positron emission tomograph. *IEEE Trans. Nucl. Sci. 36* (1989), 1020–1023.

[151] Yngwe, U. *Labelling of various macromolecules using positron emitting* ^{76}Br *and* ^{68}Ga. Dissertation, Uppsala University, Uppsala, Sweden, 2001.

[152] Zanzonico, P. B. Internal radionuclide radiation dosimetry: a review of basic concepts and recent developments. *J. Nucl. Med. 41* (2000), 297–308.

[153] Zweit, J. Radionuclides and carrier molecules for therapy. *Phys. Med. Biol. 41* (1996), 1905–1914.